FABRICATION, ORDERING AND OPTICAL PROPERTIES OF PHOTONIC CRYSTALS PREPARED FROM CRYSTALLINE COLLOIDAL ARRAYS

by

Justin Jeffrey Bohn

B.S., Cleveland State University, 2003

Submitted to the Graduate Faculty of

Arts and Sciences in partial fulfillment

of the requirements for the degree of

Doctor of Philosophy

University of Pittsburgh

2010

UNIVERSITY OF PITTSBURGH

ARTS AND SCIENCES

This dissertation was presented

by

Justin Jeffrey Bohn

It was defended on

February 22, 2010

and approved by

Sachin Velankar, Associate Professor, School of Engineering

Nathanial Rosi, Assistant Professor, Department of Chemistry

David Waldeck, Professor: Department Chair, Department of Chemistry

Dissertation Advisor: Sanford Asher, Distinguished Professor, Department of Chemistry

FABRICATION, ORDERING AND OPTICAL PROPERTIES OF PHOTONIC

CRYSTALS PREPARED FROM CRYSTALLINE COLLOIDAL ARRAYS

Justin Jeffrey Bohn, PhD

University of Pittsburgh, 2010

We developed novel understandings pertaining to the ordering and optical properties of crystalline colloidal array (CCA) materials and applied these understandings to develop novel non-close-packed inverted photonic crystal materials. CCA materials are highly charged electrostatically stabilized colloidal particles in water which readily form face centered cubic or body centered cubic lattice structures. Because their periodicity is on the order of the wavelength of light, CCA materials have the ability to Bragg diffract light in the UV, visible and NIR regions of the electromagnetic spectrum.

We utilized time resolved normal incidence reflection spectroscopy to probe the degree and kinetics of CCA ordering during the CCA crystallization process. Bragg diffraction interference fringe intensity is used to qualitatively determine the overall CCA ordering between CCA samples which have incremental additions of added ionic impurity.

We defined the physical mechanism for anomalous reflection peaks obtained in the specular reflection direction from photonic crystal materials. We utilize variable angle specular reflection spectroscopy to probe angular ranges about the normal to the (111) planes of an fcc CCA to monitor the dispersion of anomalous reflection peaks. We correlated these reflection peaks to the diffraction from higher order Miller index crystal planes through Bragg's Law. We explain the origin of these peaks as the result of a multiple diffraction process whereby light is first Bragg diffracted into a beam from a set of higher order Miller index planes and

consecutively diffracted by the in plane (111) periodicity into the (111) specular reflection direction.

We also uncovered a novel use for CCA and PCCA materials allowing us to fabricate a *non-close-packed* inverted photonic crystal material. Our novel fabrication method consists of an infiltration and condensation of a sol-gel precursor into the hydrogel matrix of a PCCA and then the subsequent removal of the PCCA material. We show that the original high ordering of the CCA is maintained through and in-depth study which examining the (111) in-plane ordering. Tuning the CCA particle number density, prior to the fabrication process provides the ability to readily tune the Bragg diffracted wavelength of the final inverted photonic crystal.

TABLE OF CONTENTS

LIST OF TABLES

LIST OF FIGURES

PREFACE

I would like to thank my research advisor, Dr. Sanford A. Asher from providing me the opportunity to do research in his laboratory. It has been a challenging, yet enlightening experience. I would also like to thank my committee members Dr. Velankar, Dr. Rosi and Dr. Waldeck fro their support through the completion of my degree.

Special thanks go out to my dear friend and colleague Dr. Alexander (Sasha) Tikhonov who has given me the pleasure of countless enlightening conversations about not only science but life as well. I have never in my life met a more patient, intelligent and down-right genuine individual like Sasha. I can only hope that we will continue to have many more "Photonic Band Damn" discussions or get the chance to collaborate in the future. Sasha you are truly one of a kind and have made me a better scientist as well as person. I cannot thank you enough. I would also like to thank my peers who have come and gone such as Matti Ben-Moshe, Jeremy Walker, Kyle Kimble and Michelle Muscatello; I am so grateful for you guidance and friendship.

I would like to thank my parents Cheryl and Jeff and my two wonderful little sisters Nikki and Andy for their endless support through everything. As a graduate student we deal not only with difficult scientific problems but hardships outside scholastics as well. Through all of my tough times you have been there to see me through the rough patches. I am so lucky to have such a great family in my life and cannot wait to spend more time with you now that this period

of my life is over. To my grandma Dorothy and grampa Emil, the little "explicative" who caused so much trouble and snuck a swig of moldy slivovitz from your leather bottle has finished his PhD.

Lastly, I would like to thank my partner in crime, Allyson Rice, for always being there for me. Through everything you have been there with a smile on your face. You have been my rock throughout these years and I couldn't have done it without you. Thank you for being so patient and understanding. You are absolutely amazing!

1.0   INTRODUCTION

For millions of years nature has possessed the ability to fabricate periodic structures which are able to control the propagation of light. These intricate structures are found in the iridescent wings of a butterfly[1] or opalescent earth-mined opals[2] and are defined as photonic crystal materials (figure 1.1)Second paragraph.
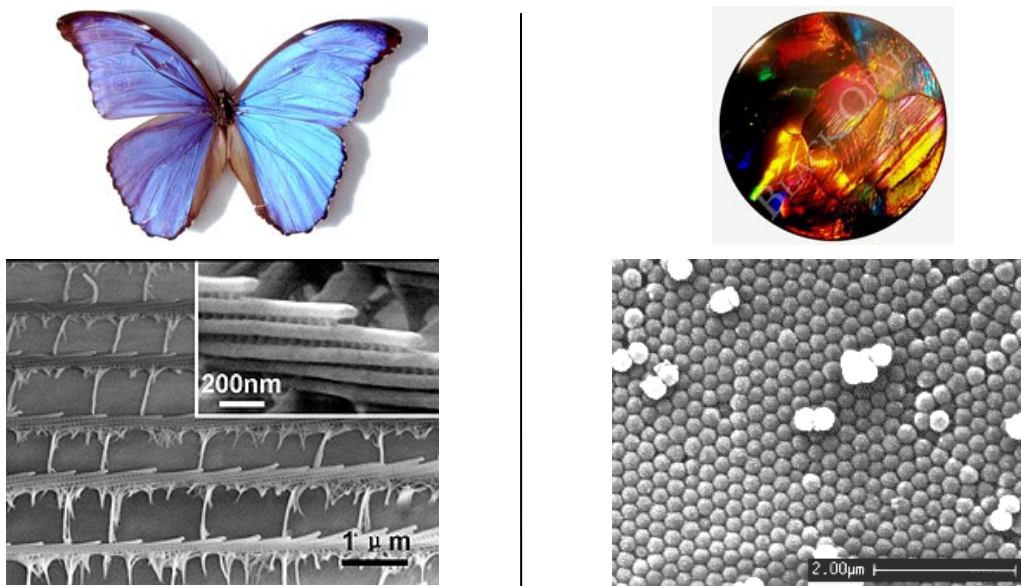
Figure 1-1 (a) The morpho butterfly is shown with a respective scanning electron micrograph of its wing. The micrograph details the intricate nanoscale periodicities which result in the iridescent color of the butterfly wing.[1] (b) An opal is shown displaying a brilliant opalescence due to the ordered silica spheres which are imaged in a scanning electron micrograph of the opal.

A photonic crystal material controls the propagation of light as the result of an inherent one, two or three dimensionally periodic modulation of refractive index contained within the crystal.[3-7] Today, man-made photonic crystals are manufactured through the self assembly colloidal particles or nano-lithographic templating. Photonic crystals are currently being employed for use in novel optical devices such as sensors, switches, filters, and coatings. Future suggested uses of these materials in optical computing require low cost manufacturing as well as ultra high crystalline order.

Colloidal crystals, are receiving a great deal of attention due to their low cost and ease of fabrication.[8, 9] Typically they are constructed in close-packed or non-close-packed fashions using a range of self assembly methods such as gravity sedimentation,[10-13] convective assembly[13-16] (close-packed) or electrostatic self assembly[17-21](non-close-packed).

Construction of a perfectly periodic, single colloidal crystal represents a major challenge in the colloidal crystal fabrication processes.[13] Native defects in the crystal structure which occur during the colloidal crystal fabrication process are vacancies, dislocations and stacking faults. Colloidal particle charge and size polydispersity will perturb the long range ordering of the colloidal crystal.[22] High colloidal particle number density can also place the crystal in an amorphous glassy phase where the ordering kinetics are slow to nonexistant.[23-25]

Small amounts of disorder in colloidal crystals is damaging to their optical properties. Interruptions in the periodic modulation of the refractive index caused by disorder decreases their diffraction efficiency.[22, 26, 27] Disorder also inhibits the formation of complete photonic band gap materials which can diffract a finite spectral bandwidth of radiation at any incident angle.[9, 28, 29] Thus, investigations focused on the improvement of colloidal crystal ordering and

the effects of ordering on their optical properties are at the forefront of colloidal crystal research.[22, 30-39]

The Asher Research Group at the University of Pittsburgh has made significant contributions to the advancement of colloidal crystal fabrication and research through the development and characterization of the Crystalline Colloidal Array (CCA).[6, 18-20, 40-47] These novel CCA materials are non-close-packed, electrostatically stabilized colloidal crystals which efficiently diffract ultraviolet, visible, and near infrared light.

CCA materials have also been used to fabricate the Polymerized Crystalline Colloidal Array (PCCA) which is composed of a CCA in an expandable/shrinkable hydrogel matrix.[48] The utility of diffractive PCCA materials is shown through their novel sensing motifs to detect significantly relevant analytes such as glucose[49-52], cations[53-55], ammonia[56], pH[57, 58], organophosphates[59, 60] and creatine[61] as well as for the formation of solid inverted photonic crystal materials. Second paragraph.

1.1   COLLOIDAL PARTICLE FORMATION / CCA SELF-ASSEMBLY

Highly charged polystyrene colloidal particles utilized in this work to fabricate CCA materials are spherical in shape and monodisperse in size.   Synthesis of these colloidal particles is carried out through a free radical emulsion polymerization technique.[42] Typically, an oil-in-water based emulsion is utilized to generate particle sizes which can be readily tuned from 100 nm to 350 nm. The standard reactants charged in the emulsion include a slightly water soluble monomer and sulfonated co-monomer, emulsifier, buffer, and a thermally active free radical initiator.   The

tunability of colloidal particle size is achieved by varying the concentrations of the emulsifier and/or the monomer

In a typical synthesis of colloidal particles having a diameter of 150 nm a jacketed, 3-neck, split-head round bottom reaction vessel (Kimble Kontes) is connected to a mechanical stirrer and temperature control unit (NESLAB RTE-211).[40] The standard setup of a typical colloidal particle polymerization reaction is shown in Figure 1.2. Next, ~175 grams of nanopure deionized water and ~0.25 grams of sodium bicarbonate (Fisher) are added in the reaction vessel and purged with nitrogen for approximately 20 minutes. The surfactant MA80 (Cytec) is then added to the reaction mixture (22 grams of 10% (w/v) MA80 in water), and oxygen is purged with nitrogen. Styrene (~96 grams) is purged with nitrogen for 20 min and added to the reaction vessel and stirred at 250 rpm. After the reaction mixture has had time to homogenize (approximately 10 minutes), ~5.2 grams of COPS 1 (Rhone-Poulenc) is added to the reaction mixture. Once the COPS 1 is added, the reaction is heated to 70 ºC and the intiator (1.2 grams ammonium persulfate in 3 ml of water) is added to the reaction. The reaction is allowed to proceed for 4 hours under constant stirring.
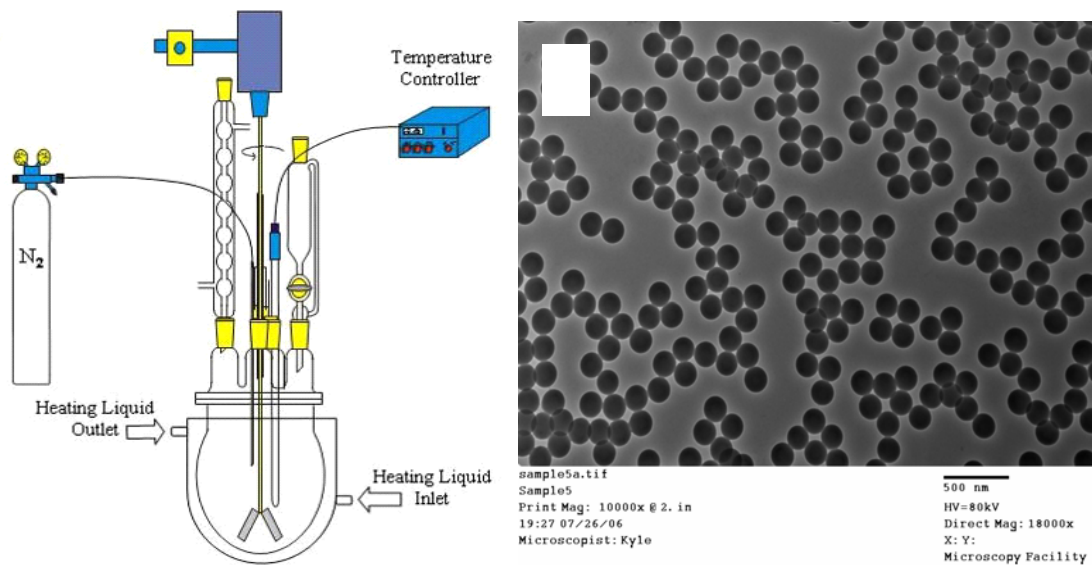
Figure 1-2 Typical polymerization reaction setup and TEM of resulting particles.

When the reaction is complete, the reactor is cooled down to room temperature and the contents are filtered through nylon mesh (Small Parts, Inc.). The colloidal particles are then dialyzed against nanopure deionized water using 10,000 molecular weight cut-off PVDF dialysis tubing (Spectrum Laboratories) for two weeks. The water used for dialysis is changed twice daily. After dialysis the colloidal particles are shaken with AG 501-X8 mixed-bed ion-exchange resin to remove excess ionic impurities (Bio-Rad).

Upon removal of the excess ionic impurities in the aqueous colloidal dispersion the electrostatic the repulsion forces between highly charged colloidal particles become large and occur over long distances (~1 μm). These large spherically symmetric electrostatic repulsion forces between colloidal particles force the colloidal dispersion to minimize its energy to form a CCA (figure 1.3). CCA will self assemble into non-close-packed face-centered cubic (fcc) or body centered cubic (bcc) arrays depending on the colloidal particle number density (figure

5

1.3).[62, 63] The center to center spacing between the colloidal particles upon CCA formation is commonly more than twice the colloidal particle diameter.
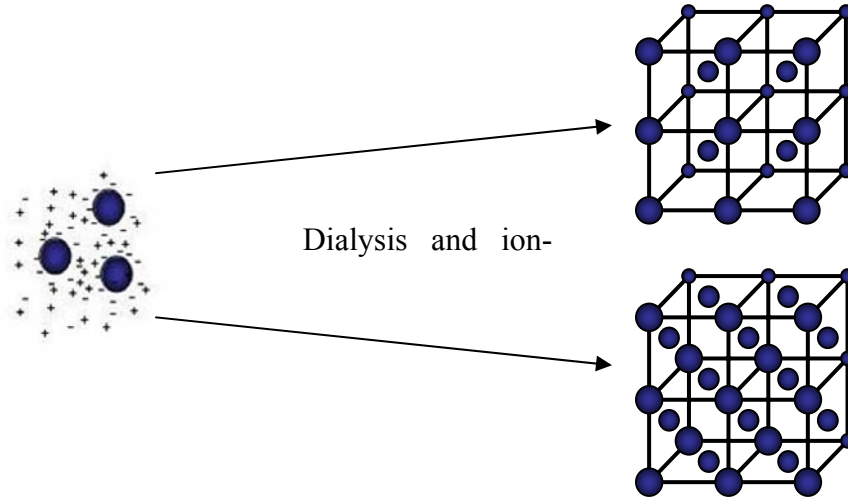
Figure 1-3 Removal of ionic impurities from the colloidal dispersion increases the electrostatic repulsive forces between colloidal particles. The strong repulsion forces between colloidal particles forces the system to minimize its energy by forming an ordered bcc (top) or fcc (bottom) array.

The electrostatic repulsion interactions between charged colloidal particles can be modeled using DLVO theory.[13, 64]   The electrostatic repulsion potential between two colloidal particles is defined in equation (1) as a function of the number of surface charge groups (Z), the Coulombic value per charge (*e*), the permittivity of vacuum (ε_o) and its scalar multiplier for solvent correction (ε_γ), the center-to-center interparticle spacing (r), the particle radius (α) and the Debye-Hückel parameter (κ).

$$U(r) = \frac{Z^2 e^2}{\varepsilon_\circ \varepsilon_\gamma} \left[\frac{e^{\kappa\alpha}}{1+\kappa\alpha} \right]^2 \frac{e^{-\kappa r}}{r}$$

Equation 1-1

$$\kappa = \sqrt{\frac{4\pi e^2}{\varepsilon_\circ \varepsilon_\gamma k_B T}\left(n_p Z + n_i\right)}$$

Equation 1-2

The Debye-Hückel parameter as defined in equation (2) is governed by the solvent dielectric constant ($\varepsilon_{o*}\varepsilon_\gamma$), the particle surface charge (Z), the particle concentration (n_s) and the ionic strength of the carrier medium (n_i). The reciprocal of the Debye-Hückel parameter, ($1/\kappa$), is the Debye length which is a measure of the colloidal particle double layer thickness. The Debye screening length decreases with increasing ionic impurity decreasing the interparticle repulsion forces.

1.2   DIFFRACTION FROM CCA

Self assembly of a CCA is clearly visible as a result of the brilliant diffraction from the ordered colloidal array (figure 1.2.1). CCA diffraction in figure 1.4 is a result of constructive interference of scattered light from the highly ordered CCA fcc (111) planes which orient parallel to the container surface. The diffracted wavelength from the fcc CCA can be tuned from blue to red by decreasing the colloidal particle number density. This can be readily achieved by increasing the volume of water which the CCA can occupy. This uniformly increases the center-to-center spacing between particles and thus, increases the spacing between fcc (111) planes. This process is also reversible, where removal of water by gentle heating will decrease the volume occupied by the CCA and therefore uniformly decrease the colloidal particle spacing.

7
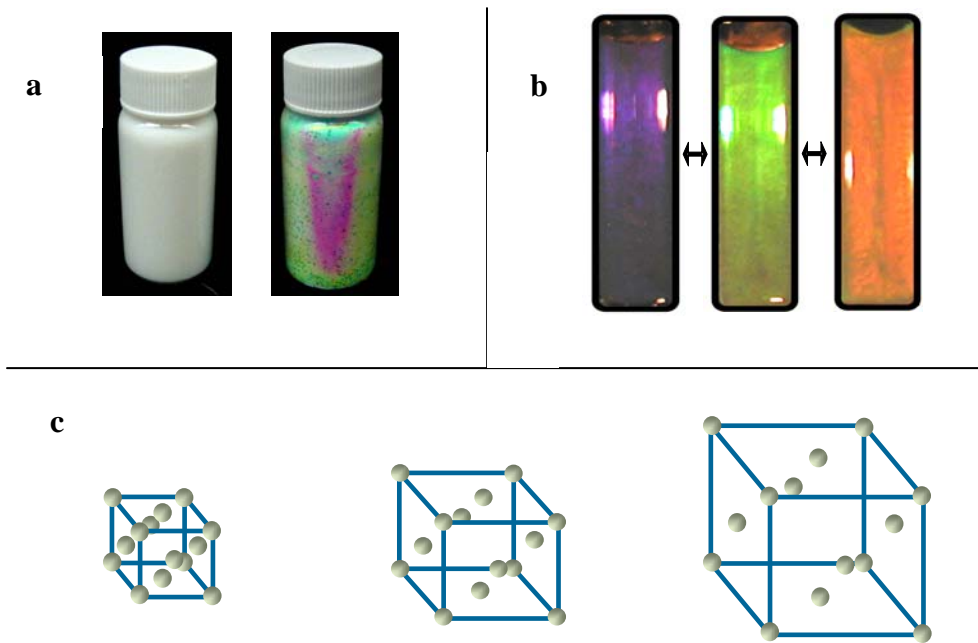
Figure 1-4 (a) Shows a dispersion of colloidal particles prior to the removal of excess ionic impurities and the resultant CCA after the colloidal dispersion has been dialysed and shaken in mixed bed ion exchange resin. (b) Shows the tunability of the CCA Bragg diffracted wavelength through the dilution or concentration of the CCA. (c) Shows the respective CCA particle spacing of figure (b) where the smallest spacing is representative of the violet CCA.

The first and most simplistic theoretical treatment of CCA diffraction can be described by Bragg's Law. Bragg's law states that for a parallel series of crystal planes with some defined inter-plane spacing there is a specific angle of incidence which generates constructive interference of incident light. In the case of colloidal crystals, the periodic planes of particles act as partially-reflecting mirrors where the spacing between the planes is on the order of the wavelength of incident light.[5-7, 19, 47]

A second, more accurate treatment of photonic crystal diffraction invokes a parallel to that which atoms have on light propagating through an atomic crystal structure.[65] Atoms in a

crystal lattice provide a refractive index mismatch from vacuum and therefore provide periodic centers for x-ray radiation to scatter. Without a mismatch from vacuum, light would propagate through the material without any disturbance. In a similar manner, photonic crystals have periodically-ordered scattering centers but on the order of the wavelengths of ultraviolet, visible, or infrared light. This extension to the Bragg case additionally assumes that light is no longer specularly reflected but scattered by centers located within periodic crystal planes, giving rise to interference effects and will be shown analogous to the Bragg case.

The kinematic theory of diffraction defines the conditions required to obtain constructive interference for a single scattering approximation.[65] This theory begins by making a series of assumptions regarding light scatter from colloidal particles. First, every particle in a photonic crystal is identical in shape, size and composition. Second, the propagation of a plane wave into the crystal generates scattering from these colloidal particles which is elastic so that there is no energy loss. With these assumptions in hand, we present the Laue conditions for diffraction.
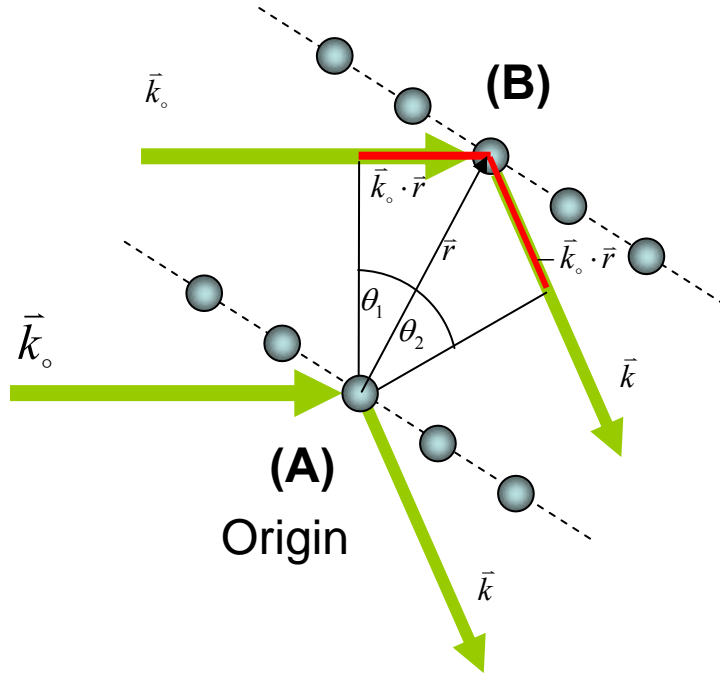
Figure 1-5 Two points in space on parallel planes scatter light in the direction of k. The extra phase accumulated from the point away from the origin is marked in red. These particles scatter light in all directions, but we are only concerned with developing the foundation for constructive interference so inclusion of it is unnecessary at this time.

The simplest case to consider is that of light striking two scattering centers (labeled A and B) located on parallel planes separated by some distance $d_{(hkl)}$ (Figure 1.5). One point is chosen as the origin (**A**) and the vector

$$\vec{r} = u\vec{a} + v\vec{b} + w\vec{c}$$

Equation 1-3

defines the position (**B**) in real space relative to this origin. After a scattering event, a relative phase change (shown in red) will occur between the two diffracted beams for a specific direction due to an extra path length traversed from the plane wave scattered from a colloidal particle

deeper in the crystal. The incident and scattered wave vectors in Figure 1.5 are labeled $\vec{k}_\circ$ and $\vec{k}$ respectively and have magnitude $1/\lambda$. The phase accumulated by the light scattered from point **B** compared to point **A** (which we label the origin) is found through the projection of $\vec{r}$ onto $\vec{k}_\circ$ and $\vec{r}$ onto $\vec{k}$ (shown in red). This yields:

$$\vec{k}_\circ \cdot \vec{r} = \vec{r} \cos\theta_2 \qquad\qquad \vec{k} \cdot \vec{r} = \vec{r} \cos\theta_1$$

Equation 1-4

where $\theta_1 = \theta_2$. The total phase accumulated is given by

$$2\pi\left(\vec{k} \cdot \vec{r} - \vec{k}_\circ \cdot \vec{r}\right)$$

Equation 1-5

We state that we are observing the interference of these two scattered waves in the far-field limit. Neglecting the differences between vectors which define subtle changes in angle from light scattered by the origin and light scattered from a point other than at the origin, equation (5) may be simplified to equation (6)

$$\text{phase} = \left[2\pi\left(\Delta\vec{k} \cdot \vec{r}\right)\right] \text{ where } \Delta\vec{k} = \vec{k} - \vec{k}_\circ.$$

Equation 1-6

The total phase is now simply the projection of $\vec{r}$ onto $\Delta\vec{k}$, where $\Delta\vec{k}$ has magnitude

$$\left|\Delta\vec{k}\right| = \frac{1}{d_{(hkl)}}$$

Equation 1-7

and direction normal to the set of parallel planes in which the two points are located in. This statement is suggested for the constructive interference case. Because the particles scatter in all directions, the direction of the scattering vector will encompass the entire sphere. The scattering vector $\Delta\vec{k}$ can be thought of as a vector which imparts a change in direction of the incident beam.

This vector direction is critical in that only specific directions of scatter yield a phase accumulation of 2π. Only in these directions will the superposition of waves scattered from lattice points in a crystal with respect to a defined origin constructively interfere. These specific directions are defined by the Laue conditions for diffraction:

$$\vec{a}\cdot\Delta\vec{k} = 2\pi q \quad \vec{b}\cdot\Delta\vec{k} = 2\pi v \quad \vec{c}\cdot\Delta\vec{k} = 2\pi s \,,$$

Equation 1-8

where $\vec{a}$, $\vec{b}$ and $\vec{c}$ are the real space lattice vectors that define a position in space relative to the origin, $\Delta\vec{k}$ is the scattering vector and q, v, and s are integer values.

These directions also arise for the Bragg Law of diffraction,

$$m\lambda = 2n_{avg}d_{(hkl)}\sin\theta \,,$$

Equation 1-9

where m is the diffraction order, λ is the wavelength, $d_{(hkl)}$ is the inter-plane spacing (where the h, k and l subscripts denote the Miller indexed plane) and θ is the glancing angle of an incident light relative to the normal of the Bragg planes of interest.

The Bragg law of diffraction assumes that an incident plane wave is specularly reflected from a series of crystal planes. The Bragg case for diffraction is depicted in Figure 1.6. When the wavelength of the incident light is on the order of the periodic spacing of the Bragg planes (where $\lambda = 2d_{hkl}$ for normal incidence), a superposition of these reflected waves generates constructive interference. As one changes the glancing angle of normal incidence from the normal of a series of planes, the wavelength required to satisfy the Bragg law will blue shift.
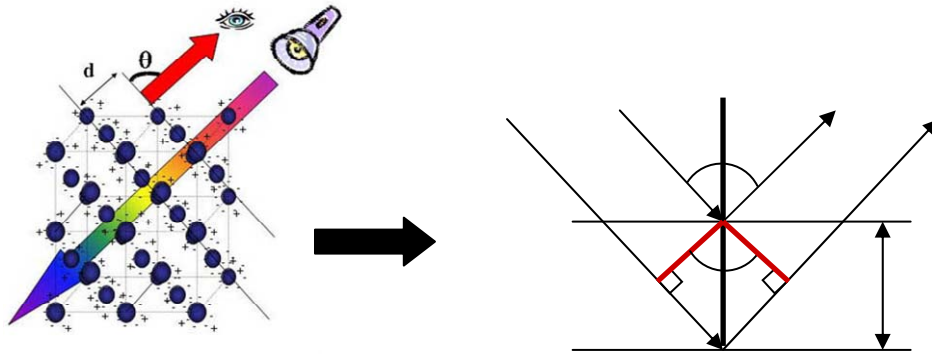
Figure 1-6 The Bragg law states that light incident upon parallel planes will constructively interfere when the extra distance traveled at some glancing angle to the normal these planes generates a path length difference of an integral multiple of λ.

The average refractive index term (n_{avg}) incorporated into the Bragg Law is a weighted average of refractive index material in the colloidal crystal. This assumption states that the average velocity of light through the crystal is represented by equation (10)

$$n_{avg} = \varphi_1 n_1 + (1 - \varphi_1)n_2 = \frac{c_{vac}}{c_{media}},$$

Equation 1-10

where φ_1 is the volume fraction of medium 1, n_1 is its respective refractive index, and n_2 is the refractive index for medium 2. For instance, a lattice plane spacing of 200 nm and colloidal crystal of $n_{avg} = 2$ would require 800 nm light at normal incidence for a Bragg diffraction event to occur. A $n_{avg} = 2$ decreases the wave velocity in the periodic media by a factor of two, which is equivalent to halving the wavelength of light. We assume that the refractive index of the

material is completely real, ignoring any loss effects due to dispersive or absorptive properties of the media.

1.3   THE POLYMERIZED CRYSTALLINE COLLOIDAL ARRAY

Although CCA are robust under conditions of low ionic strength, charge screening from ionic impurities decreases the electrostatic interaction potential raises the systems energy, destabilizing the fcc array. To circumvent this stability issue, non-ionic monomers can be polymerized in the interstitial space to lock the resulting CCA into place. This produces a PCCA (Figure 1.7).[66, 67]

The resulting PCCA has two important capabilities. First, the CCA embedded in the hydrogel matrix diffracts light according to Bragg's Law. Second, the hydrogel component provides a means of uniformly swelling and shrinking the volume of the PCCA, thereby changing the CCA lattice plane spacing and ultimately allowing the control of the Bragg diffraction wavelength.
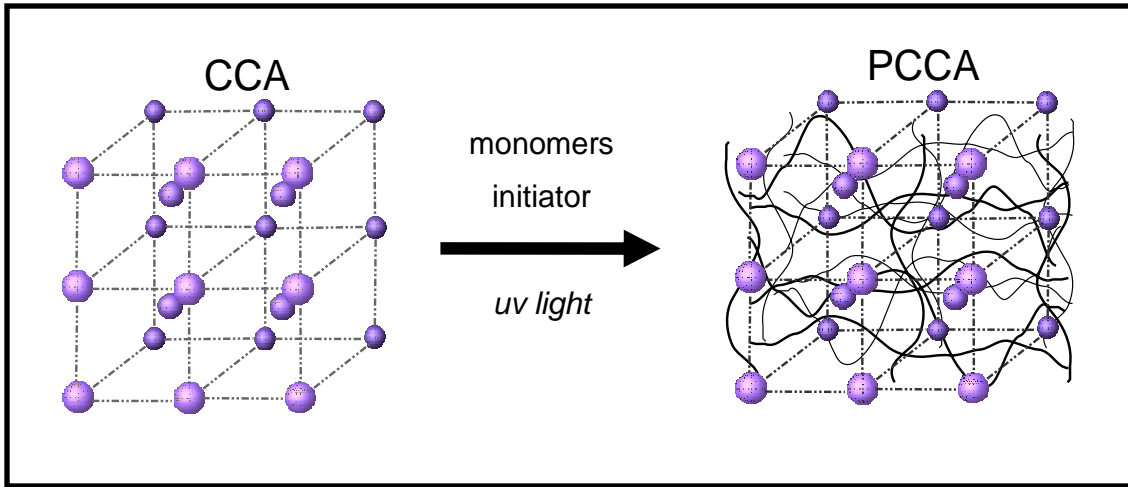
Figure 1-7 Depiction of CCA prior to and after a hydrogel matrix is polymerized into the interstitial space to form a PCCA.

The swelling and shrinking of the PCCA is described by the Flory-Huggins theory. Volume changes in the PCCA are attributed to changes in the volume derivative of two Gibbs free energies: the free energy of mixing (ΔG_M), and the free energy of elasticity (ΔG_E).[68] The former takes into account the polymer/solvent interaction and the latter allows for the elastic restoring forces inherent to the cross-linked polymer network.

The volume derivative of the sum of these two free energies generates the total osmotic pressure (Π_T) of the system which describes the swelling or shrinking of the PCCA (Equation 11).

$$\Pi_T = \Pi_m + \Pi_E = \left(\frac{\partial \Delta G_M}{\partial V} \right) + \left(\frac{\partial \Delta G_E}{\partial V} \right)$$

Equation 1-11

The changes in osmotic pressure generate volume phase transitions which can swell or shrink the hydrogel component of the PCCA.

The free energy of mixing (ΔG_m) is separated into an entropic component and an enthalpic component. The entropic component describes the number of states which may be occupied by the polymeric chains that make up the polymer matrix. The enthalpic component results from an interplay between three interaction energies: solvent-solvent interaction, polymer-polymer interaction, and solvent-polymer interaction. These three interaction energies are represented by the Flory-Huggins parameter χ, a constant which defines the energy difference between the solvent-polymer interaction and the average of the solvent-solvent/polymer-polymer interactions (equation 12).[68]

$$\chi = \frac{1}{k_B T}\left(\omega_{sp} - \frac{w_{ss} + w_{pp}}{2} \right)$$

Equation 1-12

Here (k_B) is Boltzmann's constant, (T) is the temperature of the system, (ω_{sp}) is the solvent polymer interaction and (ω_{ss}) and (ω_{pp}) are the solvent-solvent and polymer-polymer interaction energies.

When the polymer-solvent interaction is large, the hydrogel will swell. Conversely, if the polymer-solvent interaction energy is unfavorable the solvent-solvent and the polymer-polymer interactions dominate the system and therefore decreasing the volume occupied by the hydrogel.

Because the hydrogel is a large cross-linked macromolecule, there is also a restoring force which opposes swelling. This contribution is described by the free energy of elasticity. Two hydrogels having the same polymer content but a different number of effective cross-links, for example, will swell or shrink to different extents. A gel with more cross-links will be more rigid, decreasing the elasticity of the system and generating a smaller volume phase transition than that seen for a gel with a smaller number of effective cross-links. Essentially, a balance

between the free energies of the system dictates the final state of the hydrogel and, therefore, the PCCA lattice plane spacings.

PCCA's have previously been used for sensing applications due to their swelling properties which expand and contract the lattice plane spacings upon free energy changes.[69] Using these polymer-solvent interactions, we will show in this work that incorporation of inorganic material into the PCCA hydrogel backbone is a new and novel technique for the fabrication of inverted photonic crystal materials.

1.4   SYNTHESIS OF PCCA

In a typical synthesis, 2 grams of dialyzed and ion-exchanged colloidal particles are added to a 2 dram vial. Polyethylene glycol dimethacrylate (0.52 grams, Biosciences) is added to 2,2-hydroxyethyl methacrylate (3.00 grams, Biosciences).   Aluminum oxide is added to the monomer mixture to remove inhibitor, and the mixture is then centrifuged down to separate the monomer mixture from the aluminum oxide. The cleaned monomer mixture (0.5 grams) is added to the colloidal particles as well as 15 μL photo-initiator (10% diethoxyacetophenone in DMSO (w/v)), then mixed on a rotating wheel.

After it has been well mixed (~ 20 min), the CCA/monomer mixture is injected between two quartz plates and placed in a UV-polymerization chamber (Figure 1.8).   The monomer/colloid mixture is polymerized using 365 nm UV light from two mercury lamps (Black Ray) for 12.5 min. The resulting PCCA is then removed from the quartz plates, placed in water and allowed to equilibrate.
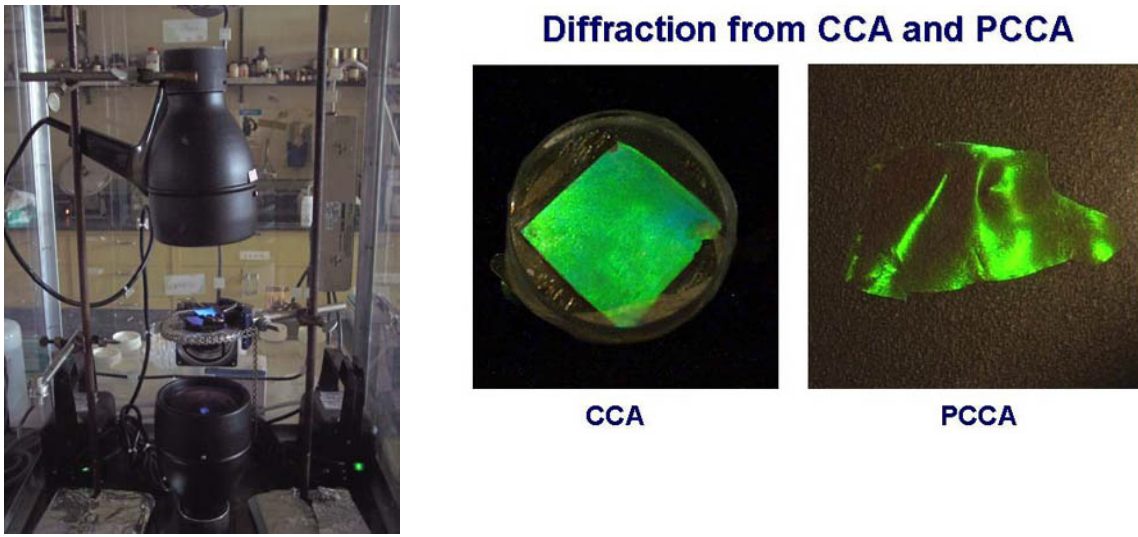
Figure 1-8 An image of the UV-polymerization chamber (left) and an image of the CCA/monomer mixture inside a quartz cell and to the right of it a PCCA in water after polymerization (right).

1.5   OVERVIEW OF RESEARCH PROGRAM

The work reported herein discusses the advancements made in the understandings of CCA ordering and the effects of ordering on CCA photonic properties. Utilizing these understandings, this work outlines the development and characterization of a novel photonic material fabricated from highly ordered CCA's.

Chapter 2 describes the monitoring of crystal growth kinetics during the crystallization of a shear melted crystalline colloidal array (CCA). The fcc CCA heterogeneously nucleates at the flow cell wall surface. We examined the evolution of the (111) Bragg diffraction peak, and, for the first time, quantitatively monitored growth by measuring the temporal evolution of the Bragg diffraction interference fringes. Modeling of the evolution of the fringe patterns exposes the

time dependence of the increasing crystal thickness. Between 80 to 90 μM NaCl concentrations the fcc crystals grow at rates between 1.9 and 4.2 μm/sec until they contact homogeneously nucleated crystals in the bulk. At lower salt concentrations crystal nucleation is slow because the shear prepared disordered phase is a glass because the strong electrostatic interactions between particles result in high activation barriers, preventing annealing. The fcc crystals melt to a liquid phase at >90 μM NaCl concentrations. Increasing NaCl concentrations slows the fcc CCA growth rate in accordance with the expectation of the classical Wilson-Frenkel growth theory.

Chapter 3 describes how angularly resolved reflection measurements suggest that higher order Miller index crystal planes of a fcc photonic crystal reflect specularly about the normal to the (111) planes. We suggest that this phenomenon results from a two step diffraction process where light is first Bragg diffracted by higher order Miller index crystal planes and is then 2D diffracted by periodicities within the (111) planes to produce the specularly diffracted light. This phenomenon is a 3D analog of the well known Wood's anomaly

Chapter 4 describes the development of a straightforward method to form non- close-packed highly ordered fcc direct and inverse opal silica photonic crystals. We utilize an electrostatically self assembled crystalline colloidal array (CCA) template formed by monodisperse, highly charged polystyrene particles. We then polymerize a hydrogel around the CCA (PCCA) and condense the silica to form a highly ordered silica impregnated (siPCCA) photonic crystal. Heating at 450 ºC removes the organic polymer leaving a silica inverse opal structure. By altering the colloidal particle concentration we independently control the particle spacing and the wall thickness of the inverse opal photonic crystals. This allows us to control the optical dielectric constant modulation in order to optimize the diffraction; the dielectric constant modulation is controlled independently of the photonic crystal periodicity. These fcc photonic

crystals are better ordered than typical close-packed photonic crystals because their self assembly utilizes soft electrostatic repulsive potentials. We show that colloidal particle size and charge polydispersity has modest impact on ordering, in contrast to that for close-packed crystals.

1.6   REFERENCES

(1)   Srinivasarao, Chem. Rev. **1999**, 99 1935.

(2)   J. B. Jones, J. V. Sanders, and E. R. Segnit, Nature (London) **1964**, 204 990.

(3)   S. John, Phys. Rev. Lett. **1987**, 58 2486.

(4)   E. Yablonovitch, Journal de Physique, Colloque **1987**, C5 C5.

(5)   M. R. D. Joannopoulos John D., Winn Joshua N., *Photonic Crystals: Moulding the Flow of Light* (Princton University Press, New York, 1995).

(6)   S. A. Asher, ((University of Pittsburgh, USA). Application: EP

EP, 1986), p. 36 pp.

(7)   C. Kittel, *Introduction to Solid State Physics* (John Wiley and Sons Inc., New York, 1968).

(8)   V. L. Colvin, MRS Bulletin **2001**, 26 637.

(9)   G. A. Ozin and S. M. Yang, Adv. Func. Mater. **2001**, 11 95.

(10)   K. E. Davis, W. B. Russel, and W. J. Glantschnig, J. Chem. Soc. **1991**, 87 411.

(11)   H. Miguez, C. Lopez, F. Meseguer, et al., Appl. Phys. Lett. **1997**, 71 1148.

(12)   A. Van Blaaderen and P. Wiltzius, Adv. Mater. (Weinheim, Ger.) **1997**, 9 833.

(13)   Y. Xia, B. Gates, Y. Yin, et al., Adv. Mater. (Weinheim, Germany) **2000**, 12 693.

(14)   Z. Zheng, X. Liu, Y. Luo, et al., Appl. Phys. Lett. **2007**, 90 051910/1.

(15)   S. Wong, V. Kitaev, and G. A. Ozin, J. Am. Chem. Soc. **2003**, 125 15589.

(16)   P. Jiang, J. F. Bertone, K. S. Hwang, et al., Chem. Mater. **1999**, 11 2132.

(17)   P. A. Hiltner and I. M. Krieger, J. Phys. Chem. **1969**, 73 2386.

(18)   R. J. Carlson and S. A. Asher, Appl. Spectrosc. **1984**, 38 297.

(19)   P. L. Flaugh, S. E. O'Donnell, and S. A. Asher, Appl. Spectrosc. **1984**, 38 847.

(20)   S. A. Asher, P. L. Flaugh, and G. Washinger, Spectroscopy (Springfield, Oreg.) **1986**, 1 26.

(21)   D. J. W. Aastuen, N. A. Clark, L. K. Cotter, et al., Phys. Rev. Lett. **1986**, 57 1733.

(22)   R. Rengarajan, D. Mittleman, C. Rich, et al., Phys. Rev. E **2005**, 71 016615/1.

(23)   P. N. Pusey and W. Van Megen, Nature (London) **1986**, 320 340.

(24)   D. Hone, S. Alexander, P. M. Chaikin, et al., J. Chem. Phys. **1983**, 79 1474.

(25)   F. Sciortino and P. Tartaglia, Adv. Phys. **2005**, 54 471.

(26)   B. Li, J. Zhou, L. Li, et al., Appl. Phys. Lett. **2003**, 83 4704.

(27)   A. Tikhonov, R. D. Coalson, and S. A. Asher, Phys. Rev. B **2008**, 77 235404/1.

(28)   S. Noda, K. Tomoda, N. Yamamoto, et al., Science (Washington, D. C.) **2000**, 289 604.

(29)   A. Blanco, E. Chomski, S. Grabtchak, et al., Nature (London) **2000**, 405 437.

(30)   V. N. Astratov, A. M. Adawi, S. Fricker, et al., Phys. Rev. B **2002**, 66 165215/1.

(31)   A. V. Baryshev, V. A. Kosobukin, K. B. Samusev, et al., Phys. Rev. B **2006**, 73 205118/1.

(32)   J. F. Galisteo Lopez and W. L. Vos, Phys. Rev. E **2002**, 66 036616/1.

(33)   U. Gasser, E. R. Weeks, A. Schofield, et al., Science **2001**, 292 258.

(34)   K. Ito, H. Nakamura, H. Yoshida, et al., J. Am. Chem. Soc. **1988**, 110 6955.

(35)   E. Palacios-Lidon, B. H. Juarez, E. Castillo-Martinez, et al., J. Appl. Phys. **2005**, 97 063502/1.

(36)   B. V. R. Tata and S. S. Jena, Solid State Commun. **2006**, 139 562.

(37)   B. V. R. Tata and B. Raj, Bull. Mater. Sci. **1998**, 21 263.

(38)   Y. A. Vlasov, V. N. Astratov, A. V. Baryshev, et al., Phys. Rev. E **2000**, 61 5784.

(39)   Y. A. Vlasov, M. Deutsch, and D. J. Norris, Appl. Phys. Lett. **2000**, 76 1627.

(40)   E. Reese Chad and A. Asher Sanford, J. colloid interface sci. **2002**, 248 41.

(41)   X. Xu, S. A. Majetich, and S. A. Asher, J. Am. Chem. Soc. **2002**, 124 13864.

(42)   C. E. Reese, C. D. Guerrero, J. M. Weissman, et al., J. Colloid Interface Sci. **2000**, 232 76.

(43)   G. Pan, A. S. Tse, R. Kesavamoorthy, et al., J. Am. Chem. Soc. **1998**, 120 6518.

(44)   J. M. Weissman, H. B. Sunkara, A. S. Tse, et al., Science (Washington, D. C.) **1996**, 274 959.

(45)   R. Kesavamoorthy, S. Tandon, S. Xu, et al., J. Colloid Interface Sci. **1992**, 153 188.

(46)   P. A. Rundquist, S. Jagannathan, R. Kesavamoorthy, et al., J. Chem. Phys. **1991**, 94 711.

(47)   P. A. Rundquist, P. Photinos, S. Jagannathan, et al., J. Chem. Phys. **1989**, 91 4932.

(48)   J. H. Holtz and S. A. Asher, Nature (London) **1997**, 389 829.

(49)   L. Alexeev Vladimir, S. Das, N. Finegold David, et al., Clin. Chem. **2004**, 50 2353.

(50)   V. L. Alexeev, A. C. Sharma, A. V. Goponenko, et al., Anal. Chem. **2003**, 75 2316.

(51)   S. A. Asher, V. L. Alexeev, A. V. Goponenko, et al., J. Am. Chem. Soc. **2003**, 125 3322.

(52)   M. Ben-Moshe, L. Alexeev Vladimir, and A. Asher Sanford, Anal. Chem. **2006**, 78 5149.

(53)   C. E. Reese and S. A. Asher, Anal. Chem. **2003**, 75 3915.

(54)   J. T. Baca, D. N. Finegold, and S. A. Asher, Analyst (Cambridge, U. K.) **2008**, 133 385.

(55)   S. A. Asher, A. C. Sharma, A. V. Goponenko, et al., Anal. Chem. **2003**, 75 1676.

(56)   K. W. Kimble, J. P. Walker, D. N. Finegold, et al., Anal. Bioanal. Chem. **2006**, 385 678.

(57)   K. Lee and S. A. Asher, J. Am. Chem. Soc. **2000**, 122 9534.

(58)   X. Xu, V. Goponenko Alexander, and A. Asher Sanford, J. Am. Chem. Soc. **2008**, 130 3113.

(59)   J. P. Walker and S. A. Asher, Anal. Chem. **2005**, 77 1596.

(60)   J. P. Walker, K. W. Kimble, and S. A. Asher, Anal. Bioanal. Chem. **2007**, 389 2115.

(61)   C. Sharma Anjal, T. Jana, R. Kesavamoorthy, et al., J. Am. Chem. Soc. **2004**, 126 2971.

(62)   Y. Monovoukas and A. P. Gast, J. Colloid Interface Sci. **1989**, 128 533.

(63)   S. Hachisu, Y. Kobayashi, and A. Kose, J. Colloid Interface Sci. **1973**, 42 342.

(64)   S. H. Behrens, D. I. Christl, R. Emmerzael, et al., Langmuir **2000**, 16 2566.

(65)   G. Subramanian, V. N. Manoharan, J. D. Thorne, et al., Adv. Mater. (Weinheim, Germany) **1999**, 11 1261.

(66)   G. Pan, R. Kesavamoorthy, and S. A. Asher, Phys. Rev. Lett. **1997**, 78 3860.

(67)   G. Pan, R. Kesavamoorthy, and S. A. Asher, Journal of the American Chemical Society **1998**, 120 6525.

(68)   P. J. Flory, **1953**.

(69)   S. A. Asher, J. Holtz, L. Liu, et al., J. Am. Chem. Soc. **1994**, 116 4997.

2.0   COLLOIDAL CRYSTAL GROWTH MONITORED BY BRAGG DIFFRACTION

INTERFERENCE FRINGES

Bohn J., Tikhonov A., Asher, S., *Submitted to Journal of Colloid and Interface Science*.

We monitor the Bragg diffraction interference fringes from a CCA in normal incidence reflection spectroscopy during the crystallization process. We show that the evolution of this interference pattern is dependant upon the electrostatic repulsion forces between colloidal particles and allows for the extrapolation of data concerning crystal thickness as well as crystal ordering.

Work done on the simulation of scattering from alternating crystal planes was done by Alexander Tikhonov. My contributions included design of the experimental setup, acquisition and analysis of data.

2.1   INTRODUCTION

Charged, monodisperse colloidal particles suspended in relatively pure water can form randomly dispersed suspensions, crystalline colloidal arrays (CCA) or they can form glassy structures.[1-9] Surface charged monodisperse colloidal particle suspensions will crystallize into non-close-

packed CCA with fcc or bcc structures over wide ranges of particle concentrations, surface charge densities and salt concentrations.[5, 6] The samples can be polycrystalline or they can form large single crystal domains.[10-15] The degree of CCA ordering depends upon the colloidal particle size and charge, as well as the particle size and charge monodispersity, the average spacing between particles and the solution ionic strength, the temperature and the medium dielectric constant, all of which impact the electrostatic interactions between particles.[16-20]

Very low particle charge and/or very high charge screening can result in particle repulsive interactions so small that the thermal kinetic energy of the particles exceeds their primary interparticle repulsive energy barriers. This allows the attractive van der Waals forces to dominate, which results in irreversible particle flocculation.[21, 22]

Increasing particle charge will electrostatically stabilize colloidal particle dispersions, preventing particle flocculation. For modest electrostatic stabilization the colloidal particles will not show long range order and, thus, adopt a liquid-like phase with short range ordering.[1, 2, 13, 23, 24] At larger electrostatic interactions the particles can self assemble into well-ordered CCA.[1, 13, 14, 25] The equilibrium particle ordering in this case is generally in an fcc or bcc structure.

Further increases in particle electrostatic interactions can create systems where the interparticle repulsive interactions are too large for the particles to crystallize into highly ordered crystalline states.[4, 7-9, 26-28] This is because the electrostatic interactions are too large to allow the particle motion and density fluctuations which enable crystal annealing. The system in this case forms a vitreous glass or an amorphous solid.[4, 7, 9, 26-28]

The kinetics of ordering of these glassy and amorphous solid systems can be very slow to nonexistent.[4, 7, 26, 27] However, these systems can be induced to order by applying mechanical perturbations such as shear forces parallel to the container walls that induce particle layer

assembly parallel to the walls; the shear forces overcome the activation barriers for particle motion. [Dozier][9, 13, 14, 29-34]

Previous studies of colloidal crystal growth in strongly electrostatically repelling colloidal suspensions show two regimes, linear growth followed by ripening. In the linear crystal growth regime the growth kinetics are controlled by particle diffusion from the melt to the growing colloidal crystal surface. The growth rates of homogeneously nucleated crystals have been measured over a large range of colloidal particle volume fractions as well as increasing salt concentrations at constant colloidal particle volume fractions.[13, 30-32, 35]

The growth rates of bcc CCA heterogeneously nucleated at the container cell wall have been measured and found to vary between 0.1 and 10 μm/s for colloidal suspensions of 102 nm diameter particles and 450 charges.[36, 37] Increasing the volume fraction of these colloidal particles from 0.0013 to 0.0024 increases the growth rate 1000-fold from .01 μm/s to 10 μm/s. Increasing the NaCl concentration from 0 μM to 1.2 μM, while holding the colloidal particle volume fraction fixed decreases the colloidal crystal growth rate from 10 μm/s to .01 μm/s.

From these studies it appears that both homogeneously and heterogeneously nucleated colloidal crystal growth rates follow the Wilson-Frenkel growth law.[13, 30, 35, 36, 38, 39] There are fewer studies of the growth rates of more strongly electrostatically interacting particles that commonly form fcc CCA.

An understanding of the crystal growth mechanisms of CCA is important for optimizing this growth to form large single domain crystals for use as photonic crystals.[11, 40-44] Thin films of these crystals can be used to reject narrow bandwidths of light from the UV to near IR spectral regions.[11, 44]

Numerous methods have been used to study the degree of ordering of CCA. Methods utilizing confocal and visual microscopy are able to image colloidal particles in the first few layers of a colloidal crystal.[36, 45-48]

The CCA Bragg diffraction intensities and bandwidths can provide information on the crystal ordering.[49-54] In the thick crystal limit a decreasing crystal ordering results in a decrease in the Bragg peak intensity and an increase in the angular width. For example, Colvin et al showed that the Bragg diffracted intensities decrease for close-packed CCA fabricated with increasing colloidal particle size polydispersities.[49] Norris et al. demonstrated for solid close packed CCA that the interference fringe modulation depths decrease with incrrsding disorder.[55] In the work here, we examine the growth kinetics of CCA formed from highly charged colloidal particles in suspensions containing different NaCl concentrations. We observe for the first time Bragg diffraction fringes from non-close packed liquid CCA samples. We use these interference fringes to monitor the growth of the CCA out from the wall where they heterogeneously nucleate.

2.2   MATERIALS AND METHODS

Our CCA are composed of 200 ± 3 nm diameter polystyrene colloidal particles (2.52×10^{13} particles/cm^3) which each possess 33,000 surface sulfonate groups. We added NaCl to the particle dispersions to partially screen the electrostatic interactions in order to achieve ordering kinetics in the sec time frame, which is easily studied.

We previously characterized the structure of our CCA without adding NaCl and found them to be fcc.[56] Since the (111) plane diffraction wavelength did not change with NaCl

addition no transition to a bcc structure occurred, indicating that the samples studied here are all in an fcc structure; if an fcc to bcc phase transition occurred due to the NaCl induced decrease in the electrostatic repulsions between particles the Bragg peak wavelength would have blue shifted ~25 nm.

We monitored the ordering and growth of CCA from the wall by measuring the relative intensities of the Bragg fcc (111) diffraction peaks and the interference fringes in the wings of these Bragg diffraction peaks. The fringe spacings are known to depend upon the crystal thickness.[55, 57] Thus, measurements of the fringe spacings directly indicate the thickness of the growing CCA crystals. As far as we know this is the first report to observe these fringes in liquid CCA samples and the first to utilize their time dependent spacings to monitor CCA growth kinetics.

Fig. 1 shows the reflection spectrum of an fcc CCA sample of 200 ± 3 nm diameter polystyrene colloidal particles containing 30 μM NaCl illuminated with a collimated white light beam normal to the flow cell container wall, where the light was collected in a backscattering geometry.

We mechanically perturbed this sample by inducing shear flow and then tapped on the container to mechanically disturb the CCA to speed up its crystallization. The peak centered at $\lambda_B = 861$ nm derives from 1st order Bragg diffraction from the fcc CCA (111) planes.

On both sides of the 1st order Bragg diffraction reflection peak we observe intensity oscillations which damp off at wavelengths away from the Bragg maximum.[49, 55, 57-59] These fringes result from the partial constructive interference for light which is back-scattered from the (111) planes within the crystal.[58]

The highest particle density fcc (111) planes orient parallel to the sample cell wall, such that normally incident light travels along the normal to the (111) planes.[2] The (111) plane diffraction occurs at $\lambda_B = 2d_{111}n_{avg}\sin\theta$, where λ_B is the wavelength of light in vacuum, n_{avg} is the CCA average refractive index, d_{111} is the (111) plane spacing and θ is the glancing angle, that for normal incidence is $\pi/2$ giving, $\lambda_B = 2d_{111}n_{avg}$. We calculate a volume averaged CCA refractive index, $n_{avg} = \varphi_{H_2O}n_{H_2O} + \varphi_{Pst}n_{Pst} = 1.357$ where φ_{H_2O} is the volume fraction and n_{H_2O} is the refractive index of water. φ_{Pst} is the volume fraction and n_{Pst} is the refractive index of polystyrene. We calculate a lattice plane spacing of $d_{111} = 321$ nm.
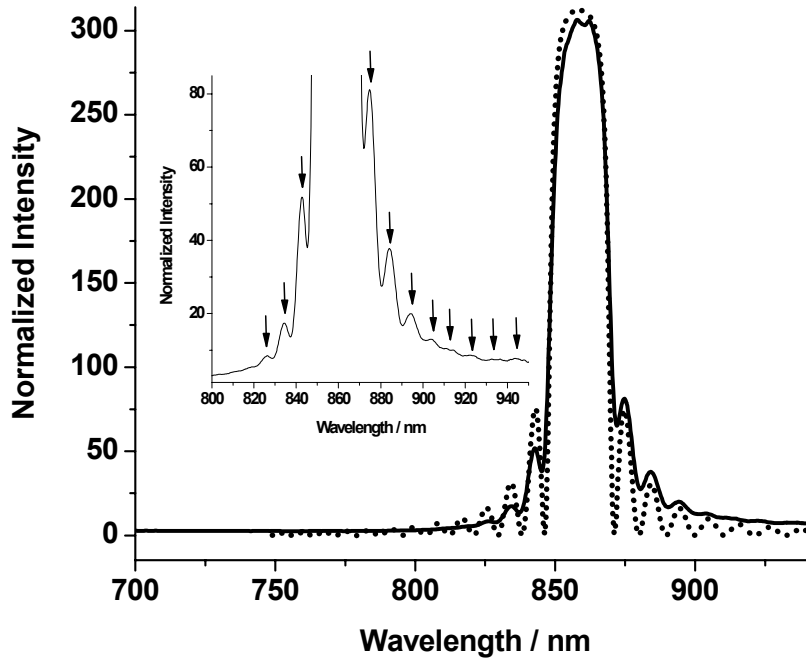
Figure 2-1 Normal incidence reflection spectrum from a CCA within a 700 μm thick flow cell. The CCA has a particle number density 23 μm^{-3} and consists of 200 ± 3 nm polystyrene particles in water containing 35 μM NaCl, where each particle contains ~33,000 surface sulfonates. The 1st order Bragg diffraction peak at normal incidence from the (111) planes occurs at 869 nm. The inset displays an expanded inset around the 1st order Bragg

diffraction peak. The dashed line shows the best fit modeling of the fringe pattern which indicates a 29 μm effective crystal thickness.

This fringe pattern can be used to determine the thickness of the CCA fcc crystal. We search for the crystal thickness which gives the best match between the calculated and observed fringe patterns. We model the CCA diffraction as if it results from a 1-D stack of bilayer dielectric slabs which have periodicities and an overall average refractive index that is identical to those of the CCA.[60] We determined the thicknesses and refractive indices of the dielectric slab bilayers by requiring them to show the same reflectance as that of a single CCA fcc (111) layer calculated in the kinematic single scattering approximation.[60] Our modeling of the Fig. 1 data indicates a total of 90 (111) layers which yields a 29 ± 0.5 μm CCA thickness.

We examined the time dependence of ordering of a CCA sample within a rectangular 700 μm flow cell. We used a syringe to inject the CCA into the flow cell and then waited until the CCA ordered to its maximum extent, as monitored by the plateauing of the increasing intensity of the (111) 1st order Bragg diffraction peak. We then perturbed the CCA ordering by injecting more sample such that the sample volume in the flow cell shifted 1 cm down the flow cell, giving a shear rate of ~14 s^{-1} for this 700 μm thick flow cell. We then monitored the diffraction evolution after this perturbation.

For our CCA samples we only observe spontaneously formed fringes in samples with NaCl concentrations between 75 to 90 μM. Samples at higher salt concentrations do not form well ordered CCA because the electrostatic interactions are too weak for long range crystalline order. Lower salt concentration samples will show fringes only if they are forced to order by repetitive shear and/or by mechanical tapping on the container wall to force ordering as in Fig. 1.

2.3   RESULTS
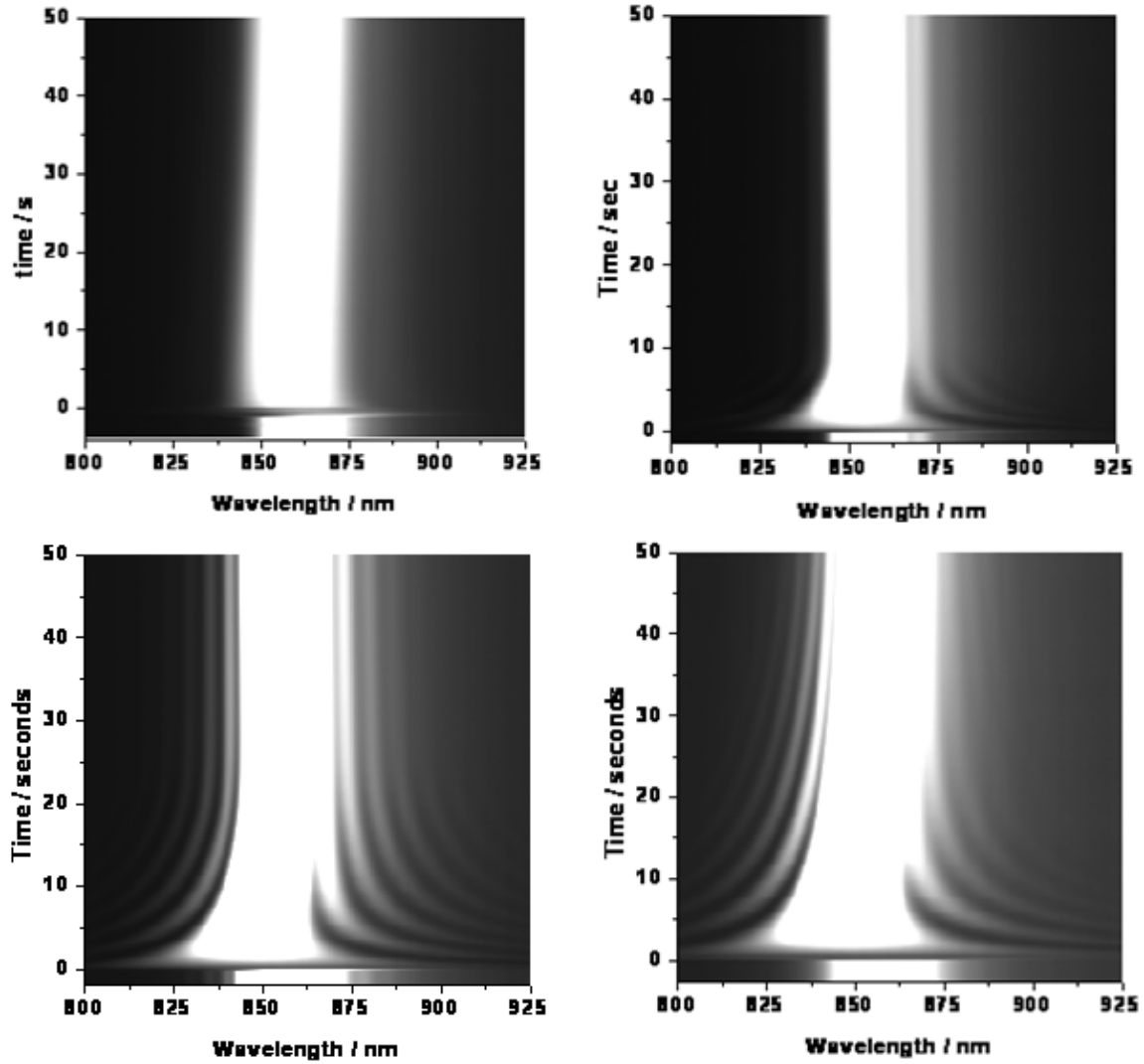
Figure 2-2: Diffraction intensity as a function of time for the 1st order Bragg diffraction from the fcc 111 planes observed at normal incidence for four CCA samples containing a 75 80, 85, and 90 µM NaCl concentrations. The data show the annealing process of the CCA after a shear flow is applied to the CCA. The lighter bands surrounding the 1st order Bragg diffraction peak show the fringe pattern evolution as the CCA thickness increases. The intensities were scaled to maximize the fringe visibility. The false color scale ranges from black to white.

31

Fig. 2 shows the time evolution of the diffraction and fringe peaks collected at normal incidence for fcc CCA samples with NaCl concentrations of 75 µM, 80 µM, 85 µM and 90 µM. The time resolved diffraction measurements are shown as overlapping diffraction spectra acquired every 0.2 sec over a one min period. We scaled the contrast of the resulting intensity profiles to visually maximize the number of interference peaks observed.
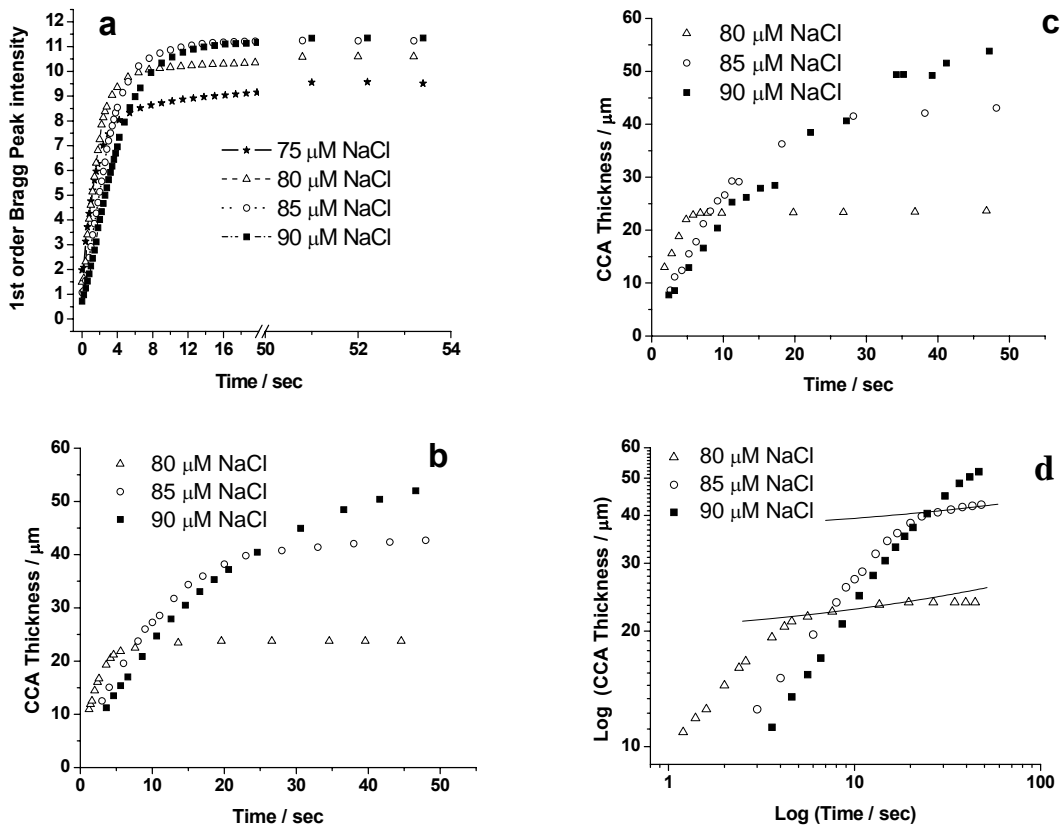
Figure 2-3 Wall crystal growth kinetics after cessation of shear flow at time zero. (a) Time dependence of Bragg diffraction peak reflected intensity for CCA containing different NaCl concentrations. (b) Modeled time dependence of calculated crystal thickness for CCA samples containing different NaCl concentrations. See text for details. (c) Time dependence of estimated crystal thickness using simplified kinematic model. See text for details. (d) log-log plot of (b).

Fig. 2 shows that the number of visible fringes increases with increasing NaCl concentrations up until 90 µM. Fringes do not spontaneously form under these shear flow conditions for NaCl concentrations below 75 µM. These colloidal particle suspensions with NaCl concentrations above 90 µM do not show formation of the diffraction peak over a period of 24 hrs after injection. A decreasing fringe spacing with an increasing fringe modulation depth indicates a growing, increasingly ordered crystal.[57]

Fig. 3a shows the 1st order Bragg diffraction peak intensities as a function of time for CCA containing 75 µM, 80 µM, 85 µM, and 90 µM NaCl concentrations. The data show an initial rapid increase in peak intensity for each CCA sample, with very similar initial rates for 75 µM and 80 µM NaCl, but with decreasing initial rates for the 85 µM and 90 µM NaCl concentrations. The largest Bragg diffraction peak intensities are achieved for the 85 µM and 90 µM NaCl concentration CCA. After ~20 sec, the 85 µM and 90 µM NaCl CCA show identical Bragg diffraction peak intensities.

Utilizing the bilayer slab modeling of the fringe pattern as discussed above as a function of time after shear perturbation we calculated the time dependence of the growing crystal thickness (Fig 3b). The 75 µM NaCl CCA sample is not included because fringes were not observed.

The fig. 3b 80 µM NaCl CCA thickness shows a rapid initial growth which stops abruptly after six sec, where the CCA achieves a final thickness of 22 ± 0.4 µm. The 85 µM NaCl CCA sample growth rate is slightly slower than that of the 80 µM NaCl CCA and saturates by ~25 sec while achieving a thickness of 43 ± 0.5 µm. The 90 µM NaCl CCA has the slowest growth rate, where the increasing thickness does not saturate within the measured 50 sec time frame. At 50 sec after shear the 90 µM NaCl CCA thickness increases to 54 ± 0.6 µm.

The reflection intensity of the main Bragg peak in Fig. 1a reaches a plateau after 5-6 sec for all our samples. However, from Fig. 3b, we see that the wall crystal thickness for the 85 and 90 μM samples continues to increase after 6 sec. The saturation of the main Bragg peak results from reaching the so-called thick crystal limit, the point at which crystal thickness is increased to the point where it diffracts essentially all incident light. Any further increase in thickness cannot affect the Bragg peak intensity. Our slab modeling of diffraction intensity shows that a perfectly ordered 16 μm thick wall crystal should diffract 90% of the incident light. This 16 μm thickness is reached after ~5 sec (Fig. 3b).

A simpler method for calculating the crystal thickness based upon a kinematic approximation gives essentially the same crystal thicknesses. In this model the intensity of the back-diffracted light is proportional to the structure factor: $S(\lambda) = [\sum_{m}^{M-1} \exp[-im(d_{111} \cdot \frac{4\pi}{\lambda})]$, where M is the number of (111) planes having a well defined inter-plane spacing. We calculate the thickness of ordered CCA along the (111) normal by calculating the number of (111) planes involved in the diffraction, which is $M = 2\pi \left\{ d_{111} n_{avg} \left(\frac{4\pi}{\lambda_1} - \frac{4\pi}{\lambda_2} \right) \right\}^{-1}$, where λ_1 and λ_2 are adjacent fringe peak wavelengths. The thickness of the ordered fcc CCA is $T = (M-1)d_{111}$. In Fig. 3c we calculated the crystal thickness by using fringe pairs furthest away from the Bragg diffraction peak. We get crystal thicknesses very similar to Fig. 3b.. The fringe pairs spacing decreases for interference fringes closer to Bragg diffraction peak because of multiple scattering effects.[58,59] Therefore, fringe pairs closer to the Bragg diffraction peak give slightly larger calculated crystal thicknesses.

2.4   DISCUSSION

2.4.1   CCA Growth

Application of shear to the CCA sample disorders the system which causes the Bragg diffraction peak to disappear. The Bragg diffraction peak reappears immediately after cessation of shear indicating prompt crystal nucleation at the wall. The Fig. 2 evolving interference fringe patterns indicate that after cessation of shear a CCA crystal of uniform thickness (over the measured 0.5 cm diameter spot size) grows out from the wall.[37] Homogeneous nucleation appears to also occur within the bulk of the colloidal suspension giving rise to growing randomly orientated CCA domains which eventually stop the growth of the wall nucleated CCA.[30, 37, 61]

The fig. 3b CCA thickness time dependence can be separated into three regions. The first region corresponds to a rapid and linear initial growth from the cell wall. These initial growth velocity decrease with increasing NaCl concentrations (4.2, 2.3 and 1.9 μm/s for the 80 μM, 85 μM, and 90 μM NaCl CCA samples).

According to classical Wilson Frenkel growth theory the growth rate follows $v=v_\infty(1-\exp(-\Delta\mu/k_BT))$ where v_∞ is the limiting velocity and $\Delta\mu$ is the chemical potential difference between the melt and the crystal. Palberg et al calculated the Wilson Frenkel growth velocity of a growing bcc CCA using the DLVO interaction potential between colloidal particles and found that the growth velocity decreases with increasing salt concentration.[36]   Our experimental observation are consistent with the Wilson Frenkel law dependence.[35, 62, 63]   The linear CCA growth is due to colloidal particle diffusion from the liquid like phase to the growing colloidal crystal surface where it adds to help grow the crystal.[13]

The wall crystal growth was measured by Wette et al in a relatively dilute system where the equilibrium crystal structure is bcc.[64] They observe a delay in the heterogeneously wall nucleated crystal growth. This may result from the requirement of a recrystallization of the flow induced rhcp structure to the final equilibrium bcc structure. Our results for a more concentrated system do not show a delay in the wall crystal growth. This could be because the evolution from the rhcp structure to the fcc structure requires only registering of the hexagonal planes. In addition, Bragg diffraction from the fcc (111) planes may not significantly differ from that of the rhcp stack.

The second region spans the time period between when the growth begins to slow and when the growth begins to stop. The slowing growth probably occurs due to contact of the growing CCA from the wall against homogeneously nucleated CCA crystallites within the bulk.[37] Fig. 3b shows that second region time span increases with increasing NaCl concentrations. At 80 μM NaCl the second time region lasts ~5 sec. For 85 μM NaCl the second growth span time interval increases to 25 sec. The time span is longest for the 90 μM NaCl CCA where the CCA thickness continues to grow past our entire measurement time period.

The CCA continues to grow out from the wall in region two even after contacting the homogeneously nucleated crystallites probably due to a crystal ripening phenomenon whereby larger CCA crystals grow at the expense of smaller CCA crystalites.[65, 66] Colloidal particles melt from smaller CCA domains and attach to larger CCA domains.[66] The particles that transfer from small to large crystallites must surmount electrostatic repulsion activation energy barriers which decrease as the NaCl concentration increases.

Thus, ripening is expected to result in the slowest further growth for the 80 μM NaCl CCA. Increasing the NaCl concentration to 85 μM and 90 μM NaCl decreases the activation

36

barriers which should increase the growth rate compared to that at lower NaCl concentrations. In region 3 the entire sample volume has crystallized, ripening has dramatically slowed because there are no small crystallites left.

Fig. 3d shows a log- log plot of the crystal thickness growth data of Fig. 3b. We find a $t^{1/3}$ power law dependence as shown by the dotted lines. The initial region of crystal growth in Fig. 3d shows a slope corresponding to a t^1 power law. The second ripening region for the 80 and 85 µM salt samples show a $t^{1/3}$ power law, which is expected for the Lifshitz-Slyozov coarsening behavior found for systems with conserved order parameters.[39,65,66] There is a transition region between the t^1 and the $t^{1/3}$ growth regions, probably because of the combination of the diffusion controlled Wilson-Frankel growth mechanism and coarsening crystal growth mechanism.[39] For the 80 µM salt sample we also see that another region at the longest times when crystal ripening growth gradually stops and the wall crystal thickness remains constant over the measured time interval. Our data for 85 and 90 µM salt samples unfortunately do not extend long enough to monitor this region where the crystal thickness stops growing.

2.4.2   CCA Ordering Quality

The number of interference fringes and their relative intensities depend on the quality of the CCA ordering. Interference fringes require that the CCA crystal has a well defined number of uniformly spaced well-ordered crystal layers. Decreasing layer ordering and uniformity will decrease the modulation of the interference fringes making them less evident.[55] Therefore, we can utilize the interference fringe pattern to monitor CCA ordering.

Interference fringes do not appear for CCA with NaCl concentrations < 75 μM in the absence of mechanical perturbations. The fringes only spontaneously appear for our CCA samples with NaCl concentrations between 80 μM to 90 μM NaCl (Fig. 2b) indicating that at these salt concentrations the CCA are able to nucleate at the wall and anneal into well-ordered crystals. The improved ordering of these CCA is also signaled by increased Bragg diffraction intensities compared to those at the lower NaCl concentration CCA. In the thick crystal limit larger Bragg intensities indicate less diffuse scattering and better crystal ordering.[67]

The 85 μM NaCl CCA shows the largest number and most modulated interference fringes indicating that it is best ordered. There are fewer, less visible fringes for the 90 μM NaCl CCA although the Bragg diffraction intensities and widths are identical. The interference fringes appear to be a more sensitive indicator of crystal order than are the Bragg diffraction intensities and bandwidths.

The decreased ordering of the higher concentration 90 μm NaCl CCA presumably results from the fact that we are approaching salt concentrations where the CCA melts. The poorer ordering of the lower salt concentration CCA in the absence of mechanical perturbation obviously results from the slow crystallization kinetics due to high activation barriers for crystallization.[45, 65, 68]

Different crystal defects can differentially impact the visibility of the interference fringes. Interference fringes become less visible if there is a variation in spacing between hexagonal layers, or if the (111) layers are distorted from the shape of an ideal plane. Thus, the fringes will become less visible if the incident light simultaneously samples several domains with a different numbers of layers. Therefore our method based on monitoring interference fringes is limited to

the single domain crystals of relatively high quality. Stacking faults and different stacking of layers will have little or no effect on interference fringes.

The lack of well ordered wall nucleated crystals for CCA samples containing NaCl concentrations below 80 μM results in a lack of visible fringes. At low salt, defects do not spontaneously anneal because the relatively high electrostatic interactions between colloidal particles freezes kinetic annealing processes. For intermediate salt concentrations the crystals can be forced to anneal by application of mechanical perturbations such as shearing and tapping. By repeated shearing and mechanical tapping we were able to obtain interference fringes for the 35 μM NaCl sample as shown in Fig. 1.

Typical light scattering experiments to determine the size of a growing crystal measures the width of the Bragg peak for a colloidal crystal having low dielectric contrast between the colloidal particles and the solvent. For these low contrast systems incident light is only weakly attenuated by the crystal. To achieve low dielectric contrast, special index matching techniques were often employed. In contrast, when the dielectric contrast becomes so large that the attenuation length is comparable with the size of a crystal, multiple scattering effects become important and crystal size can not be determined from the width of the Bragg main peak. Paradoxically the same high value of dielectric contrast, that precludes obtaining the crystal size from the width of the main Bragg peak, helps us to determine crystal thickness from spacing between interference fringes, since the higher the dielectric contrast, the higher the interference fringe intensities.

2.4.3   Bragg Diffraction Blue Shift

Upon shearing the 75 µM, 80 µM, 85 µM and 90 µM samples the Bragg diffraction peaks disappear. After shearing the Bragg peak of the growing wall nucleated CCA crystal is initially blue shifted relative to that before the shear by 2 nm, 3.5 nm, 7 nm, and 9 nm, respectively (Fig. 2). The Bragg peak then redshifts until it reaches its previous equilibrium value. This Bragg diffraction blueshift probably results from a shear flow induced colloidal particle concentration increase at the wall which equilibrates over time after cessation of shear. The concentration increase can result from the flow induced elastically strained shear layers, which was previously observed by Palberg et al.[69] The magnitude of the blue shift decreases as NaCl concentrations decrease because larger electrostatic repulsive interactions increase the resistance to particle concentration increases.

These shear induced particle concentration increases result in elastic energy storage within the CCA. After the shear forces dissipate this stored elastic energy drives the system back towards a homogeneous particle concentration, which causes the lattice constant and the resulting Bragg peak to relax back to its equilibrium value. All but the 90 µL NaCl sample fully relaxes within 1 min. The 90 µL NaCl sample takes longer probably, in part, because of its smaller Young's modulus which resulted in a larger concentration increase as indicated by the larger diffraction blueshift. In addition, it is possible that crystal melting could be involved in storing elastic energy which would give rise to a long time constant relaxation.
The relaxation back to equilibrium is similar for the 80 µM, 85 µM and 90 µM samples with a fast relaxation (~5 sec) followed by a much slower relaxation (~1 min). The 75 µM NaCl sample relaxation differs from the other samples because it continues to blueshift for ~5 sec after

cessation of shear. This suggests an additional stage of elastic response where a new source of elastically stored energy after cessation of shear continues to increase the particle concentration near the wall. We will continue to examine this process which occurs in CCA which have larger interparticle electrostatic interactions.

2.5   CONCLUSIONS

We monitored the growth of fcc CCA heterogeneously nucleated at the cell wall after shear disorder by monitoring the Bragg diffraction intensities, and for the first time, the Bragg interference fringe patterns. Modeling of the evolution of the fringe patterns exposes the time dependence of the increasing crystal thickness. Between 80 to 90 μM NaCl concentrations the fcc crystals grow from the wall at rates between 1.9 and 4.2 μm/sec until they contact homogeneously nucleated crystals in the bulk. At lower salt concentrations crystal nucleation is slow because the shear prepared disordered phase is a glass because the strong electrostatic interactions between particles result in high activation barriers preventing annealing. The fcc crystals melt to a liquid phase at >90 μM NaCl concentrations. Increasing NaCl concentrations slows the fcc CCA growth rate in accordance with the expectations of the classical Wilson-Frenkel growth theory.

2.6   AKNOWLEDGMENTS

2.7   REFERENCES

(1)   P. A. Hiltner, I. M. Krieger, *J. Phys. Chem.* 73 (1969) 2386.

(2)   R. Kesavamoorthy, S. Tandon, S. Xu, S. Jagannathan, S. A. Asher, *J. Colloid Interface Sci.* 153 (1992) 188.

(3)   R. J. Carlson, S. A. Asher, *Appl. Spectrosc.* 38 (1984) 297.

(4)   E. B. Sirota, H. D. Ou-Yang, S. K. Sinha, P. M. Chaikin, J. D. Axe, Y. Fujii, *Phys. Rev. Lett.* 62 (1989) 1524.

(5)   Y. Monovoukas, A. P. Gast, *J. Colloid Interface Sci.* 128 (1989) 533.

(6)   P. N. Pusey, W. Van Megen, *Nature (London)* 320 (1986) 340.

(7)   W. van Megen, S. M. Underwood, *Nature (London)* 362 (1993) 616.

(8)   L. Cipelletti, L. Ramos, *J. Phys.: Condens. Matter* 17 (2005) R253.

(9)   F. Sciortino, P. Tartaglia, *Adv. Phys.* 54 (2005) 471.

(10)   P. L. Flaugh, S. E. O'Donnell, S. A. Asher, *Applied Spectroscopy* 38 (1984) 847.

(11)   S. A. Asher, P. L. Flaugh, G. Washinger, *Spectroscopy (Springfield, Oreg.)* 1 (1986) 26.

(12)   T. Okubo, *Polym. J. (Tokyo, Jpn.)* 40 (2008) 882.

(13)   T. Palberg, *J. Phys.: Condens. Matter* 11 (1999) R323.

(14)   N. A. Clark, A. J. Hurd, B. J. Ackerson, *Nature (London)* 281 (1979) 57.

(15)   A. Van Blaaderen, P. Wiltzius, *Adv. Mater. (Weinheim, Ger.)* 9 (1997) 833.

(16)   A. Yethiraj, A. van Blaaderen, *Nature (London)* 421 (2003) 513.

(17)   P. Pieranski, L. Strzelecki, B. Pansu, *Phys. Rev. Lett.* 50 (1983) 900.

(18)   W. Van Megen, I. Snook, *Adv. Colloid Interface Sci.* 21 (1984) 119.

(19)   M. O. Robbins, K. Kremer, G. S. Grest, *J. Chem. Phys.* 88 (1988) 3286.

(20)   A. Yethiraj, *Soft Matter* 3 (2007) 1099.

(21)   W. B. Russel, D. A. Saville, S. W.R., Colloidal Dispersions, Cambridge University Press, New York, 1989.

(22)   P. C. Hiemenz, Principles of Colloid and Surface Chemistry, 2nd Ed.*,* Marcel Dekker, New York, 1986.

(23)   T. Okubo, *J. Phys. Chem.* 93 (1989) 4352.

(24)   J. C. Zahorchak, R. Kesavamoorthy, R. D. Coalson, S. A. Asher, *J. Chem. Phys.* 96 (1992) 6873.

(25)   R. Kesavamoorthy, B. V. R. Tata, A. K. Arora, A. K. Sood, *Phys. Lett. A* 138 (1989) 208.

(26)   P. N. Pusey, W. Van Megen, P. Bartlett, B. J. Ackerson, J. G. Rarity, S. M. Underwood, *Phys. Rev. Lett.* 63 (1989) 2753.

(27)   H. J. Schope, T. Palberg, *J. Non-Cryst. Solids* 307-310 (2002) 613.

(28)   H. J. Schope, T. Palberg, *Prog. Colloid Polym. Sci.* 118 (2001) 82.

(29)   W. Khunsin, G. Kocher, S. G. Romanov, C. M. Sotomayor Torres, *Adv. Funct. Mater.* 18 (2008) 2471.

(30)   D. J. W. Aastuen, N. A. Clark, L. K. Cotter, B. J. Ackerson, *Phys. Rev. Lett.* 57 (1986) 1733.

(31)   B. J. Ackerson, N. A. Clark, *Phys. Rev. A* 30 (1984) 906.

(32)   J. Vermant, M. J. Solomon, *J. Phys.: Condens. Matter* 17 (2005) R187.

(33)   A. Van Blaaderen, *MRS Bull.* 29 (2004) 85.

(34)   W. D. Dozier, P. M. Chaikin, J. Physique 43 (1982) 843

(35)   T. Okubo, S. Okada, *J. Colloid Interface Sci.* 192 (1997) 490.

(36)   M. Wuerth, J. Schwarz, F. Culis, P. Leiderer, T. Palberg, *Phys. Rev. E* 52 (1995) 6415.

(37)   A. Stipp, R. Biehl, T. Preis, J. Liu, A. B. Fontecha, H. J. Schoepe, T. Palberg, *J. Phys.: Condens. Matter* 16 (2004) S3885.

(38)   T. Okubo, A. Tsuchida, T. Kato, *Colloid Polym. Sci.* 277 (1999) 191.

(39)   Y. He, B. J. Ackerson, W. van Megen, S. M. Underwood, K. Schaetzel, *Phys. Rev. E* 54 (1996) 5286.

(40)   S. John, *Phys. Rev. Lett.* 58 (1987) 2486.

(41)   E. Yablonovitch, *Journal de Physique, Colloque* C5 (1987) C5.

(42)   A. Blanco, E. Chomski, S. Grabtchak, M. Ibisate, S. John, S. W. Leonardo, C. Lopez, F. Meseguer, H. Miguez, J. P. Mondia, G. A. Ozin, O. Toader, H. M. Van Driel, *Nature (London)* 405 (2000) 437.

(43)   S. Noda, K. Tomoda, N. Yamamoto, A. Chutinan, *Science (Washington, D. C.)* 289 (2000) 604.

(44)   P. L. Flaugh, S. E. O'Donnell, S. A. Asher, *Appl. Spectrosc.* 38 (1984) 847.

(45)   K. Ito, H. Nakamura, H. Yoshida, N. Ise, *J. Am. Chem. Soc.* 110 (1988) 6955.

(46)   B. V. R. Tata, B. Raj, *Bull. Mater. Sci.* 21 (1998) 263.

(47)   U. Gasser, E. R. Weeks, A. Schofield, P. N. Pusey, D. A. Weitz, *Science* 292 (2001) 258.

(48)   V. Prasad, D. Semwogerere, E. R. Weeks, *J. Phys.: Condens. Matter* 19 (2007) 113102/1.

(49)   R. Rengarajan, D. Mittleman, C. Rich, V. Colvin, *Phys. Rev. E* 71 (2005) 016615/1.

(50)   E. Palacios-Lidon, B. H. Juarez, E. Castillo-Martinez, C. Lopez, *J. Appl. Phys.* 97 (2005) 063502/1.

(51)   Y. A. Vlasov, V. N. Astratov, A. V. Baryshev, A. A. Kaplyanskii, O. Z. Karimov, M. F. Limonov, *Phys. Rev. E* 61 (2000) 5784.

(52)   V. N. Astratov, A. M. Adawi, S. Fricker, M. S. Skolnick, D. M. Whittaker, P. N. Pusey, *Phys. Rev. B* 66 (2002) 165215/1.

(53)   J. F. Galisteo Lopez, W. L. Vos, *Phys. Rev. E* 66 (2002) 036616/1.

(54)   A. V. Baryshev, V. A. Kosobukin, K. B. Samusev, D. E. Usvyat, M. F. Limonov, *Phys. Rev. B* 73 (2006) 205118/1.

(55)   Y. A. Vlasov, M. Deutsch, D. J. Norris, *Appl. Phys. Lett.* 76 (2000) 1627.

(56)   A. Tikhonov, J. Bohn, S Asher, *Phys. Rev. B* 80 (2009) 235125.

(57)   P. Jiang, J. F. Bertone, K. S. Hwang, V. L. Colvin, *Chem. Mater.* 11 (1999) 2132.

(58)   A. Yariv, Y. Pochi, Optical Waves in Crystals: Propagation and Control of Laser Radiation*,* Wiley-Interscience, New York, 1984.

(59)   H. Miguez, V. Kitaev, G. A. Ozin, *Appl. Phys. Lett.* 84 (2004) 1239.

(60)   A. Tikhonov, R. D. Coalson, S. A. Asher, *Phys. Rev. B* 77 (2008) 235404/1.

(61)   R. Blaak, S. Auer, D. Frenkel, H. Loewen, *J. Phys.: Condens. Matter* 16 (2004) S3873.

(62)   H. A. Wilson, *Philos. Mag.* 50 (1900) 238.

(63)   J. Frenkel, *Phys. Z. Sowjetunion* 1 (1932) 498.\

(64)   P. Wette, A. Engelbrecht, R. Salh, I. Klassen, K. Menke, D. M. Herlach, S. V. Roth H. J. Schope, *J. Phys.: Condens. Matter* 21 (2009)

(65)   S. Iacopini, T. Palberg, H. J. Schoepe, *Phys. Rev. E* 79 (2009) 010601/1.

(66)   S. Iacopini, T. Palberg, H. J. Schoepe, *J. Chem. Phys.* 130 (2009) 084502/1.

(67)   W. H. Zachariasen, Theory of X-Ray Diffraction In Crystals, Dover, New York, 1967.

(68)   C. Haro-Perez, L. F. Rojas-Ochoa, R. Castaneda-Priego, M. Quesada-Perez, J. Callejas-Fernandez, R. Hidalgo-Alvarez, V. Trappe, *Phys. Rev. Lett.* 102 (2009) 018301/1.

(69)   T. Palberg, R. Biehl, Faraday Discuss. 123 (2003) 133

3.0 PHOTONIC CRYSTAL MULTIPLE DIFFRACTION OBSERVED BY ANGULAR-RESOLVED REFLECTION MEASUREMENTS

We experimentally observe anomalous peaks in the specular reflection direction of a CCA. We identify the origin of these peaks as a result of a multiple diffraction process. The reflection peaks are assigned to the Miller index crystal planes from which the diffraction condition was met. We were able to detect up to eight separate higher order Miller index crystal planes which gave an anomalous reflection peak.

Contributions to this work from Alexander Tikhonov include calculation of the Bragg diffraction dispersion lines and analysis of the 2D and 3D diffraction from CCA. My contributions to this manuscript involve the studies of 2D and 3D Bragg diffraction, the experimental design and collection of spectra.

3.1   INTRODUCTION

Photonic crystal materials (PhC) are being developed for use in optical devices and for applications in optical computing and optical communications, with the expectation that photonic circuitry will replace electronic circuitry.[1]   The periodic modulations of the optical dielectric constant in these PhC materials are used to control the propagation of electromagnetic radiation at wavelengths comparable to the modulation periodicity.[2, 3]

Obviously, it is essential to develop a deep understanding of the interaction of light with these PhC materials.   Although there have been numerous studies which have examined diffraction from PhC, significant aspects of the diffraction phenomena remain unclear.

Many previous studies examined diffraction from PhC using angularly resolved reflection or transmission spectroscopy.[4-14]   These studies observed complex patterns of peaks or dips in diffraction intensities which depend upon the angle of incidence and observation.   The diffraction phenomena give rise to diffraction dispersion spectra.   Two approaches are used to rationalize the origin of these diffraction dispersion spectra.   The first relates these experimental diffraction dispersion spectra to the allowed photonic bands determined from band structure calculations.[4-7, 9-12, 15]   The second relates these diffraction dispersion spectra to the Bragg diffraction phenomena expected from particular crystal planes.[4, 6-8, 12-14]

Good correlations have been obtained between some experimental diffraction dispersion spectra and low energy photonic bands associated with diffraction from the (111) and (200) planes.[5-7, 11-14]   These lower energy photonic bands follow the wavelength versus angular dependence predicted by Bragg's law in regions away from band crossings.   However, in the region where the (111) and (200) photonic bands cross, multiple Bragg wave coupling results in the repulsion of these two bands and deviations from Bragg's law.[5]   The situation is more

complex at higher frequencies, where higher frequency dispersion lines poorly correlate to the photonic bands found from band structure calculations. [10, 11]

A number of groups examined higher energy dispersion spectra in relatively low contrast PhC and found that, in general, the dispersions can be fit to Bragg's law. Watson et al were able to fit five diffraction dispersion lines in a bcc PhC measured with transmission spectroscopy to diffraction from higher order Miller index planes.[8] Shutzmann et al[6] were able to fit four reflection diffraction dispersion lines for fcc PhC. However, they did not discuss why their higher order Bragg diffraction should occur at angles which are specular to the fcc (111) planes. Numerous groups have been trying to understand why the diffraction from higher order Miller index planes should appear specular to the (111) planes.[4-14] The explanation by Miguez et al proposes that flattening of the photonic bands as a function of wave vector **k** results in a large effective refractive index, n_{eff}, which leads to a high reflectivity at the sample surface at the Bragg diffraction condition.[10] This argument does not clarify why this diffraction would have the wavelength versus angle dependence given by Bragg's law.

We further examine these phenomena here by studying the angular resolved reflection spectra from highly ordered fcc crystalline colloidal array (CCA) PhC oriented with their (111) planes parallel to the PhC flat surface. Our low dielectric constant modulated PhC displays 8 diffraction dispersion lines; as far as we know, this is the largest number yet observed. We introduce a simple phenomenological model to explain the origin of the reflection spectroscopy peaks in the high frequency region as a multiple diffraction phenomenon.

We propose that each dispersion line occurs as a result of two consecutive scattering processes: In the first scattering process, the incident light is 3D Bragg diffracted by a set of crystal planes. In the second scattering process this Bragg diffracted wave is 2D diffracted by

48

the 2D periodicity within the surface (111) planes. The resulting diffracted light propagates as if it was specularly reflected relative to the incident light. We suggest that this phenomenon is similar to that known for 1D system as a Wood's anomaly.[16-20]

3.2   EXPERIMENTAL

In our study we examine two non-close packed fcc Crystalline Colloidal Array (CCA) samples made from 198 nm highly-charged, spherical polystyrene colloidal particles suspended in water. The particles were prepared as described elsewhere.[21] CCA self assemble due to the electrostatic repulsion between the charged particles[22] into either an fcc or bcc crystal depending on particle number density and surface charge.[23] The fcc CCA samples were injected into a 700 μm thick borosilicate glass flow cell. These CCA align their highest density (111) planes parallel to the cell surface. We measured the reflection spectra of the CCA sample for unpolarized light over the angular range of 20° to 70° about the normal to the fcc (111) planes in the LU and LW Brillouin zone rotation directions. Variable angle specular reflectance data were measured by using a Cary 5000i spectrophotometer equipped with a variable angle specular reflectance accessory (Varian Inc.). The angular resolution was set at 2°, the beam area at the CCA sample was 1 cm^2 and the collection angular aperture was 8°.

At normal incidence to the (111) planes the high particle concentration CCA sample shows the longest wavelength Bragg diffraction at 682 nm, while the low concentration CCA sample diffracts 1078 nm light. We calculated the CCA lattice constant and effective average refractive index from a linear best fit of the (111) Bragg diffraction wavelengths for different angles of incidence to the experimental lowest energy dispersion line. Fitting of the (111) Bragg

diffraction including light refraction was done assuming constant values of the refractive index of water and polystyrene. The lattice constants and effective average refractive indices were 429 nm and 1.380 for the high concentration CCA, and 695 nm and 1.343 for the low concentration CCA. We took cognizance of the wavelength dependence of the refractive index of water and polystyrene when fitting the higher order Miller index dispersion lines. We used the same fitted effective refractive index for both the Bragg's law calculation and for the Snell's law correction for refraction of incident light at the CCA surface.

3.3   RESULTS AND DISCUSSION

Fig. 1 shows the diffraction dispersion lines obtained over the LW Brillouin zone directions for the high and low concentration CCA samples. The most intense diffraction dispersion line from the (111) planes follows Bragg's law up to the (111) and (200) dispersion line crossing point.
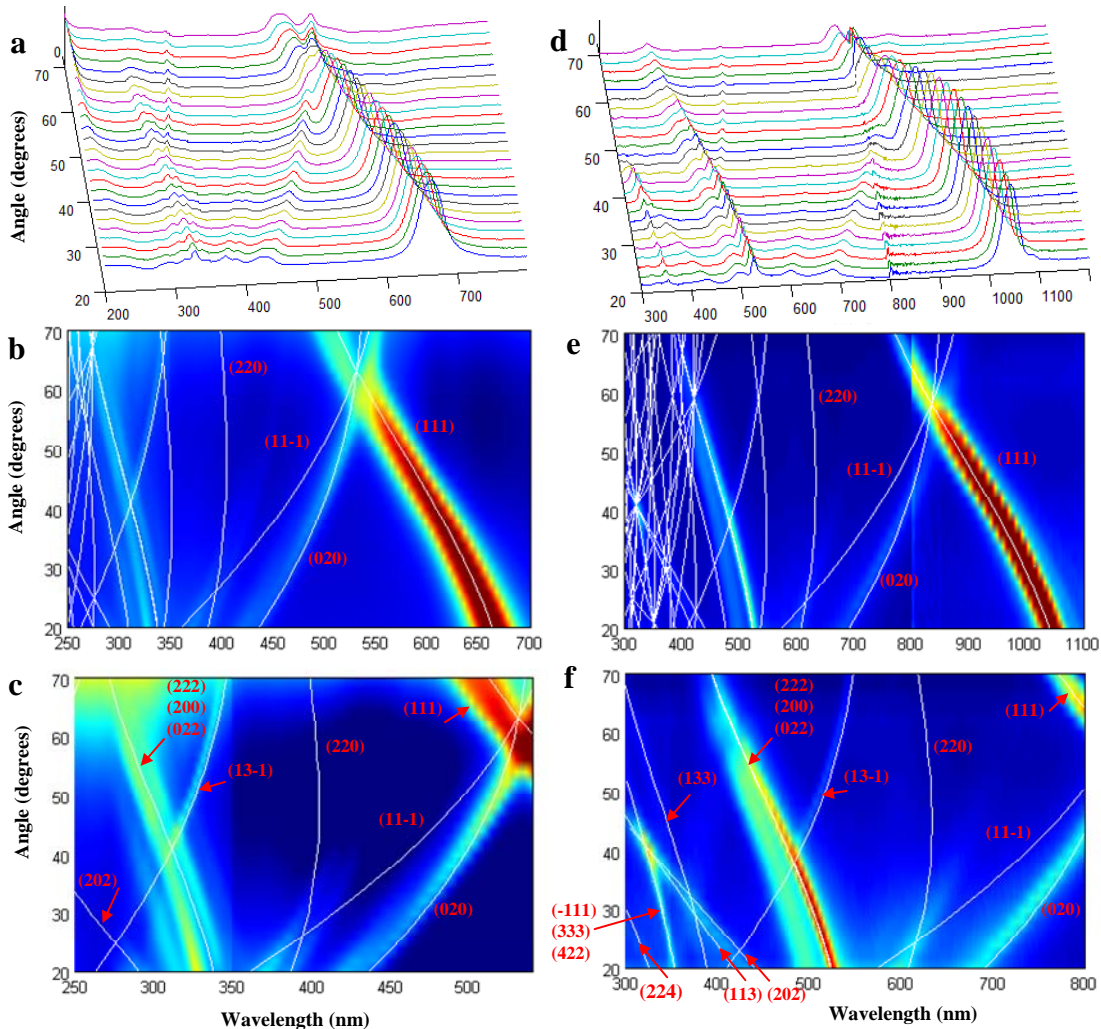
Figure 3-1 Reflection spectra along the LW Brillouin zone direction for (a-c) high concentration and (d-f) low concentration CCA. The calculated Bragg dispersions lines are plotted on the experimental data contour plots. c and f show expanded versions of b and e and show only the calculated Bragg dispersion lines that are fit to experimental data. The color map in c and f were scaled to improve the contrast and visibility of experimentally obtained dispersion lines. The step anomaly at 800 nm in d is an experimental artifact due to detector switching in the spectrophotometer.

The other dispersion lines follow Bragg's law calculated fits (white lines) as if the incident light diffracted from one of the higher order Miller index planes where the diffracted light was somehow directed in the specular reflection direction. The dispersion line fits to the

higher Miller index planes cannot simply derive from a simple 3D Bragg diffraction since the incident light would not be diffracted in the specular reflected direction.

The expected diffraction from PhC should result in bright spots at specific angular directions which overlay a diffuse background scattering from defects and disorder. These bright diffraction spots result from 3D Bragg diffraction from crystal planes and from 2D diffraction from the surface layers.

In reflection we often observe a hexagonal pattern of six 2D diffraction spots from the (111) layers near the surface. The total light intensity in each 2D diffraction spot results from partial constructive interference of diffraction by all of the (111) layers.[24] For a simple Bravais lattice, 3D Bragg diffraction can be considered as a special case of 2D diffraction where the scattered light amplitudes from every layer are in phase and constructively interfere.
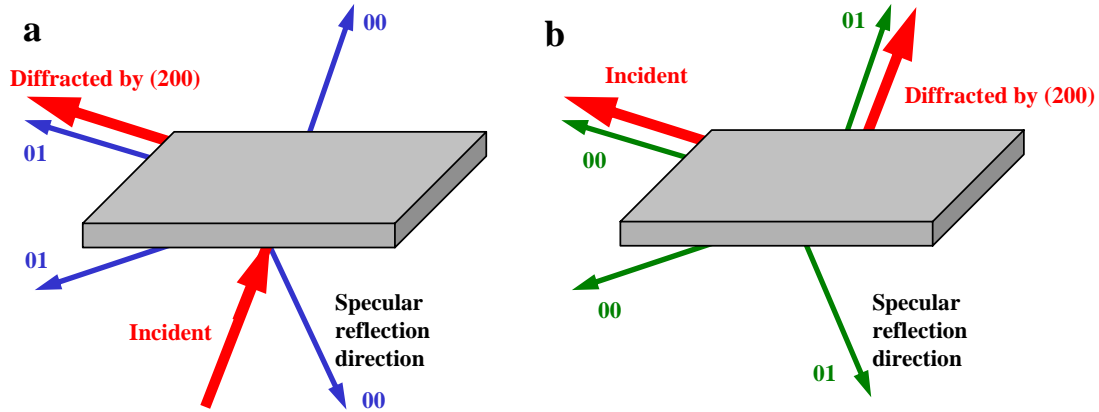
Figure 3-2 llustration of a two-step diffraction process resulting in specularly diffracted light from (200) crystal planes about the (111) surface normal. (a) In the first step monochromatic light is incident at 10° about the (111) normal onto the photonic crystal such that it Bragg diffracts from the (200) planes at 99.5° (the incident and 3D diffracted beam are shown by red arrows). The blue arrows show 2D diffraction of the incident light from the hexagonal particle arrays within the (111) planes. The 2D diffraction spectral orders are indicated. Zero order 2D diffraction occurs in the specular reflection direction. (b) In the second diffraction the 3D Bragg diffracted light by the (200) planes is subsequently 2D diffracted by the particles in the (111) planes. This subsequently 2D diffracted light (green arrows) coincides with the 2D diffraction directions in (a). The 01 order 2D diffraction exits the PhC in the direction of specular reflection about the (111) plane direction.

As shown quantitatively below, the appearance of the higher frequency specular reflection dispersion lines in Fig. 1 involves a multiple diffraction phenomenon. Two consecutive diffraction events are required for an incident monochromatic beam to diffract from a higher order Miller index planes and to exit the PhC in the specularly reflected direction about the (111) plane normal (Fig. 2). When the PhC is illuminated at the Bragg diffraction condition for a specific crystal plane, some of the incident light is redirected into a Bragg diffracted wave propagating inside the PhC. Then this wave 2D diffracts off (111) layers into several diffraction orders, one of which is diffracted into the specular reflected direction.

Fig. 2a shows the calculated 2D and 3D (200) Bragg diffracted beams for an incident monochromatic beam at an *internal* angle 10° to the (111) plane normal that is Bragg diffracted by the (200) planes. The incident beam wavevector $\vec{k}_{in}$ and the 3D Bragg diffracted beam wavevector $\vec{k}_{sc}$ define the scattering plane containing the (200) plane normal (red arrows). In addition to this 3D Bragg diffraction, weaker 2D diffraction occurs from the surface (111) planes, generating a number of 2D diffracting beams (four beams for our specific scattering geometry) with wavevectors $\vec{k}^{2D}{}_{sc}$ (blue arrows). We use the (200) set of planes as an example here, but the analyses is valid for all crystal planes.

Fig. 2 shows two first order 2D diffraction beams, one of which coincides with the (200) 3D diffraction direction. There are also two additional zero order 2D diffracted beams which propagate in the transmitted and (111) specularly reflected directions.

We will prove that if the 3D Bragg condition occurs, the 2D diffraction condition will also occur, by proving that the projection of the 3-D reciprocal lattice vector of the (200) planes, $\vec{G}_{200}$ onto the (111) plane coincides with a 2D reciprocal lattice vector within the (111) plane. We will then show that the 3D diffracted beam can be further diffracted by a 2-D reciprocal lattice vector resulting in a 2D diffracted beam which propagates as if it were specularly reflected from the (111) planes.

The 2D periodicity within a particular crystal plane is defined by two primitive 2D lattice vectors $\vec{a}$ and $\vec{b}$, while the 3D periodicity of the FCC lattice is defined by its 3D primitive lattice vectors $\vec{A}$, $\vec{B}$ and $\vec{C}$. The set of 2-D reciprocal lattice vectors, $\vec{G}^{2D}$, within a particular lattice plane satisfies the two Laue equations $\vec{a} \cdot \vec{G}^{2D} = 2\pi\, m_1$ and $\vec{b} \cdot \vec{G}^{2D} = 2\pi\, m_2$ while the 3D reciprocal lattice vectors of the 3D lattice satisfies the three Laue equations $\vec{A} \cdot \vec{G} = 2\pi\, n_1$,

$\vec{B} \cdot \vec{G} = 2\pi\, n_2$ and $\vec{C} \cdot \vec{G} = 2\pi\, n_3$. Since the individual crystal planes are part of the 3D lattice we can write $\vec{a} = a_1\vec{A} + a_2\vec{B} + a_3\vec{C}$ and $\vec{b} = b_1\vec{A} + b_2\vec{B} + b_3\vec{C}$ where (a_1, a_2, a_3) and (b_1, b_2, b_3) are integers.

Therefore:

$$\vec{a} \cdot \vec{G}^{\parallel} = \vec{a} \cdot (\vec{G} - \vec{G}^{\perp}) = \vec{a} \cdot \vec{G} = a_1\vec{A} \cdot \vec{G} + a_2\vec{B} \cdot \vec{G} + a_3\vec{C} \cdot \vec{G} = 2\pi(a_1 n_1 + a_2 n_2 + a_3 n_3) \text{ and}$$

$$\vec{b} \cdot \vec{G}^{\parallel} = \vec{b} \cdot (\vec{G} - \vec{G}^{\perp}) = \vec{b} \cdot \vec{G} = b_1\vec{A} \cdot \vec{G} + b_2\vec{B} \cdot \vec{G} + b_3\vec{C} \cdot \vec{G} = 2\pi(b_1 n_1 + b_2 n_2 + b_3 n_3) \text{ where}$$

$$\vec{G} = \vec{G}^{\perp} + \vec{G}^{\parallel}.$$

Since $(a_1 n_1 + a_2 n_2 + a_3 n_3)$ and $(b_1 n_1 + b_2 n_2 + b_3 n_3)$ are integers we have proved that $\vec{G}^{\parallel}$ satisfies the Laue equations. This verifies that the projection of $\vec{G}_{200}$ onto the (111) plane, $\vec{G}^{\parallel}_{200}$, is a 2D reciprocal lattice vector within the (111) plane.
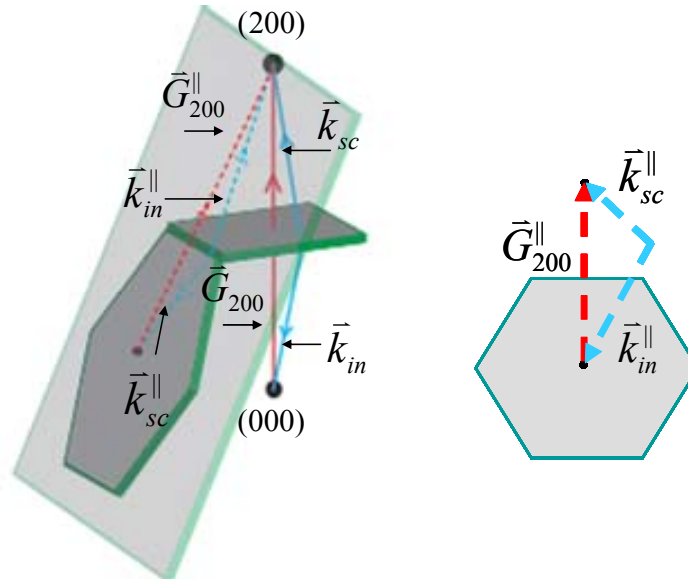
Figure 3-3(a) The fcc Brillouin zone is shown with the incident and scattered wave vectors satisfying the diffraction conditions from the (200) planes. $\vec{G}_{200}$ and the incident and scattered wave vectors are projected into the (111) plane. (b) The first Brillouin zone of the (111) planes is shown as are the projections of $\vec{G}_{200}$ into this plane. $\vec{G}^{\parallel}_{200}$ and the projections of the incident and scattered wave vectors together satisfy the 2D diffraction condition. The 2-D scattered wavevector lies parallel to the direction of projection of the 3D Bragg diffracted wavevector.

Fig. 3a shows two fcc Brillouin zone surfaces where the (111) surface lies within the rectangular plane shown. The wave vectors $\vec{k}_{in}$ and $\vec{k}_{sc}$ (blue) and $\vec{G}_{200}$ (red) satisfy the 3-D Bragg condition $\vec{k}_{sc} = \vec{k}_{in} + \vec{G}_{200}$ forming a triangle. The $\vec{G}_{200}$ reciprocal lattice vector is oriented along the ΓX direction, ending on the 200 reciprocal lattice point. Fig 3a shows the projection of these wavevectors ($\vec{k}^{\parallel}_{in}$, $\vec{k}^{\parallel}_{sc}$ and $\vec{G}^{\parallel}_{200}$) onto the (111) plane (blue dashed lines), while Fig. 3b concentrates on the 111 Brillouin zone and shows the projected wavevectors onto this surface.

The parallel projections of $\vec{k}_{in}$, $\vec{k}_{sc}$ and $\vec{G}_{200}$ onto the (111) plane forms a triangle: $\vec{k}^{\parallel}_{sc} = \vec{k}^{\parallel}_{in} + \vec{G}^{\parallel}_{200}$ This vector relation indicates the fulfillment of a 2D diffraction

condition, since $\vec{G}^{\parallel}{}_{200}$ is a 2D reciprocal lattice vector. This argument proves that the 3D diffraction from the (200) set of planes simultaneously fulfills a 2D diffraction condition within the (111) planes, where the projection, $\vec{G}^{\parallel}{}_{200}$ is the 2D reciprocal lattice vector.

The (200) diffracted beam, which for a thick photonic crystal has an intensity similar to that of the incident light, propagates within the PhC, and is subsequently diffracted by the 2-D periodicity within the (111) planes. The directions of this 2D diffraction are shown by the green arrows in Fig. 2b which lie parallel to the Fig. 2a 2D diffraction directions shown by the blue arrows.

The 2D diffraction condition is $\vec{k}^{\parallel}{}_{out} = \vec{k}^{\parallel}{}_{sc} + \vec{G}^{2D}$ where $\vec{G}^{2D}$ is a reciprocal lattice vector lying within the (111) planes. When $\vec{G}^{2D} = -\vec{G}^{\parallel}{}_{200}$ the corresponding 2D diffraction beam, $\vec{k}_{out}$, propagates in the specularly reflected direction about the normal to the (111) planes; the parallel projections of the incident and specularly reflected beam are equal, $\vec{k}^{\parallel}{}_{out} = \vec{k}^{\parallel}{}_{in}$. By combining the diffraction conditions for the first and second scattering events we obtain: $\vec{k}^{\parallel}{}_{out} = \vec{k}^{\parallel}{}_{sc} - \vec{G}^{\parallel}{}_{200} = \vec{k}^{\parallel}{}_{in} + \vec{G}^{\parallel}{}_{200} - \vec{G}^{\parallel}{}_{200} = \vec{k}^{\parallel}{}_{in}$. Therefore, the resultant diffracted beam from these two scattering events propagates in the specularly reflected direction.

Using this result we can understand the origin of the diffraction dispersion lines in Fig 1. We plot our assigned calculated Bragg dispersion lines on top of the experimentally measured reflection data. We do not observe some of the diffraction dispersion lines that we calculate probably because of their weak intensities.[25]

We observe a well resolved (020) Bragg dispersion line over the measured angular range which crosses the (111) line. The line crossing occurs at the high symmetry W-point of the Brillouin zone. The calculated and measured dispersion lines overlap completely until the crossing point, whereupon the calculated results begin to deviate significantly from those

experimentally observed. The deviation increases as the angles increase past the crossing point, as previously observed by others.[6] This deviation after the crossing point presumably results from our simplistic use of a water and polystyrene volume average refractive index in the Bragg dispersion line calculations. In addition, we ignore the fact that we are in the dynamical diffraction limit rather than in the kinematic diffraction limit.[26]

The anti-crossing behavior of (111) and (200) dispersion lines near their crossing point was studied both experimentally and theoretically by considering simultaneous diffraction by the (111) and (200) planes.[5-7, 11-14, 27] The coupling between these multiple Bragg waves and deviation of the dispersion lines from the simple Bragg's law behavior was explained as a band repulsion of the relevant Bloch eigenstates.[5] The avoided crossing interval between the dispersion lines will increase as the photonic crystal dielectric contrast modulation increases due to an increased coupling between the two Bragg diffraction waves.[5] Due to the relatively small dielectric contrast of our CCA's, we observe only a small anti-crossing behavior for the (111) and (200) dispersion lines for our high concentration sample and see little anti-crossing behavior for our dilute sample.

We see more dispersion lines then observed previously using either transmission and reflection methods using UV, visible and near IR light for both close-packed and non-close-packed PhC, for similar low dielectric constant CCA.[6, 8, 28] The increased number of dispersion lines we observe may result from better ordering of our highly charged polystyrene CCA PhC.

We also observe good fits between our calculated diffraction dispersion lines and measured dispersion lines for the (13-1), (311) (222), (200), (022), (202) and (113) crystal planes. We are also able to fit the dispersion line observed between 20° and 30° near the intersection of (220) and (11-1) Bragg lines.

Fig 1 shows two additional crossing points at the intersection of the (222) and (13-1), (311) and (113) Bragg lines. These two new dispersion line crossing points are located in the high-energy region where the opening of the FCC complete photonic band will occur for a refractive index contrast >2.8.[29]
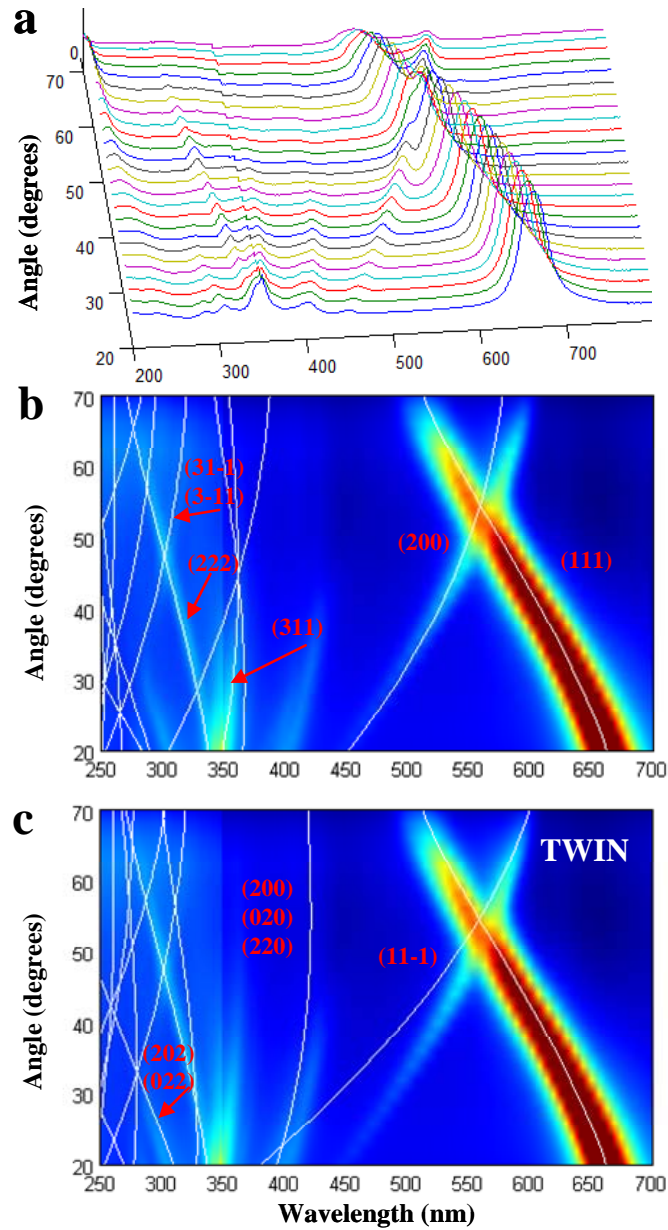
Figure 3-4 (a) Specularly reflected intensity along the LU direction for high concentration CCA. (b) The calculated Bragg dispersion overlayed onto the experimental data contour plot. (c) The Bragg dispersion calculated for twinned crystal configuration.

Fig. 4 shows reflectance spectra obtained for the high concentration CCA over the angular range 20°-70° along the LU rotation direction. Fig. 4b shows the calculated Bragg

dispersion lines together with the experimental data. Five experimental dispersion lines are in a good agreement with Bragg's law for the diffraction from (111), (200), (311), (222) and simultaneously (31-1) and (3-11) crystal planes. However, two well resolved dispersion lines remain unaccounted for. The origin of these lines is easily explained as a result from Bragg diffraction of the (200), (020), (220) and (202), (022) crystal planes of a twinned structure. The existence of dispersion lines originating from a twin structure indicates the existence of stacking faults in our CCA sample.

For the LW rotation direction the Bragg dispersion diagram for the fcc crystal and its twin are identical, unlike that for the LU rotation direction. This indicates that for the LW direction it is not possible to distinguish between the dispersion lines of the normal and twin structures.
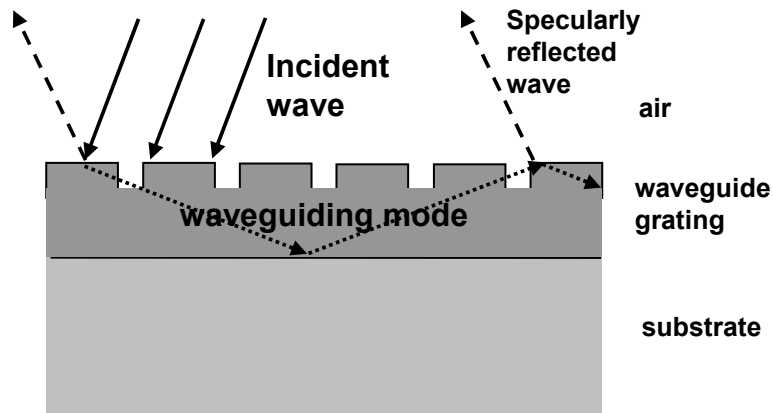
Figure 3-5 Wood's anomaly in waveguide grating structure. Light incident at waveguide grating is coupled to the waveguiding mode according to a phase matching Bragg diffraction. The waveguided mode is diffracted again by the same grating periodicity into the specularly reflected wave.

This multiple diffraction phenomenon is reminiscent the Wood's anomaly known for 1D and 2D dielectric periodic waveguiding grating structures.[17, 19] The simplest structure (Fig. 5)

which can generate a Wood's anomaly is comprised of a waveguide grating attached to a substrate. Wood's anomalies in these types of structures give rise to sharp peaks in the specularly reflected intensity for particular wavelengths of light at specific angles of incidence. Wood's anomalies are explained by the resonant coupling of the incident light wave to a guided wave which propagates along the waveguide grating. The coupling between the incident and guided waves occurs through the phase matching Bragg condition $k_G = k_{in} + K$, where k_G and k_{in} are the guided and incident wavevector projections onto the surface of the grating structure and K is the 1D grating reciprocal lattice vector. Coupling also occurs in the opposite direction, where the guided mode Bragg diffracts through the same phase matching condition, thus resulting in an intensity peak in the specularly reflecting direction.

Thus, two consecutive diffraction processes occur where the incident and diffracted beams are related through the phase matching Bragg diffraction. This mechanism is similar to our multiple diffraction model which gives rise to the reflectance peaks in angularly resolved spectra of 3D PhC.

In summary, we show that light diffracted from higher order Miller index crystal planes of a FCC photonic crystal in the specularly reflected direction about the normal to the (111) planes results from a multiple diffraction phenomenon. This phenomenon is a result of a two step diffraction process whereby light is Bragg diffracted by a higher order Miller index crystal plane and also 2D diffracted by 2D periodicities within the (111) planes. We suggest that this phenomenon is an analog of the Wood's anomaly in diffracting grating structures.

3.4   AKNOWLEDGMENTS

3.5   REFERENCES

(1)   J. D. Joannopoulos, P. R. Villeneuve, and S. Fan, Nature (London) **1997**, 387 830.

(2)   E. Yablonovitch, Physical Review Letters **1987**, 58 2059.

(3)   S. John, Physical Review Letters **1987**, 58 2486.

(4)   W. L. Vos and H. M. van Driel, Physics Letters A **2000**, 272 101.

(5)   H. M. van Driel and W. L. Vos, Physical Review B: Condensed Matter and Materials Physics **2000**, 62 9872.

(6)   S. Schutzmann, I. Venditti, P. Prosposito, et al., Optics Express **2008**, 16 897.

(7)   S. G. Romanov, T. Maka, C. M. Sotomayor Torres, et al., Physical Review E: Statistical, Nonlinear, and Soft Matter Physics **2001**, 63 056603/1.

(8)   R. D. Pradhan, J. A. Bloodgood, and G. H. Watson, Physical Review B: Condensed Matter **1997**, 55 9503.

(9)   E. Pavarini, L. C. Andreani, C. Soci, et al., Physical Review B: Condensed Matter and Materials Physics **2005**, 72 045102/1.

(10)   H. Miguez, V. Kitaev, and G. A. Ozin, Applied Physics Letters **2004**, 84 1239.

(11)   M. Ishii, M. Harada, A. Tsukigase, et al., Colloids and Surfaces, B: Biointerfaces **2007**, 56 224.

(12)   J. F. Galisteo-Lopez, E. Palacios-Lidon, E. Castillo-Martinez, et al., Physical Review B: Condensed Matter and Materials Physics **2003**, 68 115109/1.

(13)   G. M. Gajiev, V. G. Golubev, D. A. Kurdyukov, et al., Physical Review B: Condensed Matter and Materials Physics **2005**, 72 205115/1.

(14)   A. V. Baryshev, A. B. Khanikaev, H. Uchida, et al., Physical Review B: Condensed Matter and Materials Physics **2006**, 73 033103/1.

(15)   J. F. Galisteo-Lopez and C. Lopez, Physical Review B: Condensed Matter and Materials Physics **2004**, 70 035108/1.

(16)   R. W. Wood, Philos. Mag. **1902**, 4 396.

(17)   A. Hessel and A. A. Oliner, Appl. Opt. **1965**, 4 1275.

(18)   S. S. Wang, R. Magnusson, J. S. Bagby, et al., J. Opt. Soc. Am. A **1990**, 7 1470.

(19)   D. Rosenblatt, A. Sharon, and A. A. Friesem, J. Quantum Electron. **1997**, 33 2038.

(20)   S. Fan and J. D. Joannopoulos, Phys. Rev. B **2002**, 65 235112/1.

(21)   C. E. Reese, C. D. Guerrero, J. M. Weissman, et al., Journal of Colloid and Interface Science **2000**, 232 76.

(22)   P. L. Flaugh, S. E. O'Donnell, and S. A. Asher, Applied Spectroscopy **1984**, 38 847.

(23)   R. J. Carlson and S. A. Asher, Applied Spectroscopy **1984**, 38 297.

(24)   W. Loose and B. J. Ackerson, J. Chem. Phys. **1994**, 101 7211.

(25)   F. Lopez-Tejeira, T. Ochiai, K. Sakoda, et al., Phys. Rev. B **2002**, 65 195110/1.

(26)   B. T. Schwartz and R. Piestun, Journal of the Optical Society of America B: Optical Physics **2005**, 22 2018.

(27)   J. F. Galisteo Lopez and W. L. Vos, Physical Review E: Statistical, Nonlinear, and Soft Matter Physics **2002**, 66 036616/1.

(28)   I. I. Tarhan and G. H. Watson, Physical Review Letters **1996**, 76 315.

(29)   K. Busch and S. John, Physical Review E: Statistical Physics, Plasmas, Fluids, and Related Interdisciplinary Topics **1998**, 58 3896.

4.0 CHARGE STABILIZED CRYSTALLINE COLLOIDAL ARRYAS AS TEMPLATES FOR FABRICATION OF NON-CLOSE-PACKED INVERTED PHOTONIC CRYSTALS

We developed a novel, straightforward fabrication technique to produce non-close-packed inverted photonic crystal materials from a CCA template. We show the facile tunability of the non-close-packed inverted photonic crystal diffraction wavelength through simple adjustments of the CCA particle number density. We demonstrate the ability of CCA to ameliorate defects in particle size which allows for highly ordered photonic crystal materials.

In this work contributions from Alexander Tikhonov and Dan Qu involve DLVO theory modeling of 1D colloidal particle arrays. Daniel N. Lamont's contributions to this work involve modeling the pair correlation functions of 2D SEM images of CCA. My contributions to this work include the experimental design and procedure, spectroscopic studies, structure characterization, and synthesis of the non-close-packed inverted photonic crystal materials.

4.1   INTRODUCTION

The last two decades has seen the emergence of the important field of photonic crystals. The name photonic crystals was coined to describe materials which control light propagation through periodic variations in their optical dielectric constants.[1-3]

Photonic crystal materials are of major technological significance in areas such as optical computing and communications where photonic devices are being developed to replace electronic devices.[3-9] Photonic crystal materials also offer the possibility to fabricate complete 3-D photonic bandgap materials which exclude electromagnetic radiation (including the vacuum field) within its finite spectral bandgap.[10, 11] Phenomena such as spontaneous emission are suppressed in these materials.[2, 12]

Lithography is the most straightforward method to fabricate two and three dimensional photonic crystal materials for photonic applications.[13-21] This top down fabrication methodology is highly successful in fabricating complex photonic crystal materials. These fabricated structures are extremely useful in demonstrating proof of concept for photonic crystal devices. However, lithographic processes are expensive, and this cost is likely to prevent commercialization of many photonic crystal devices.

Thus, much of the recent work in photonic crystal fabrication has utilized colloidal particle self assembly. The utility of colloidal particle self assembly is evident from the photonic crystal materials found in nature. For example, earth mined opals are photonic crystals formed from the close packed self assembly of silica colloidal particles.[22] The first work fabricating artificial opals used gravity sedimentation to obtain photonic crystal periodic structures.[23-25]

Much of the recent colloidal particle self assembly work has emphasized methods that form close packed photonic crystal materials. These methods utilize variances of vertical

colloidal particle deposition methods.[26-30] Surprisingly, many of these close packed assembly methods claim formation of fcc crystals[25, 31-33] which require that the self assembly select for the fcc crystal form, rather than the random stacked crystal forms, which would normally result from simple hard sphere interparticle interactions; the fcc crystal assembly process requires long range interparticle interactions that select for fcc ABCABC layer packing.

A major limitation of close packed photonic crystal systems is that their ordering, and therefore their photonic crystal properties depend upon the colloidal particle size polydispersity. Clearly, increasing size polydispersity will degrade ordering[34]. Further, charge polydispersity will degrade ordering to the extent that electrostatic interactions are involved in the close packing mechanism. Disorder in the photonic crystals degrade the magnitude and increase the widths of the Bragg diffraction peaks.[34-36]

Fabrication of a complete 3-D photonic bandgap material requires specific crystal structures and a very large periodic variation in its optical dielectric constant. The most straightforward approach to forming a complete 3-D photonic bandgap crystal would utilize an inverse opal fcc crystal structure that requires a minimum refractive index ratio of 2.8.[37] The inverse opal structure is formed within an fcc photonic crystal by infiltrating an fcc photonic crystal structure with a high refractive index material, and then removing the original fcc spheres, leaving an inverse fcc lattice of air holes with a refractive index of n=1.

Optimization of the inverse opal crystal structure would permit decreasing the required refractive index modulation. For example, it was recently found that an inverted non close packed fcc lattice shows a wider photonic band gap (10 %) than does a close packed inverted fcc crystal structure with the same lattice constant.[38, 39]

The recent work which has attempted to generate non close packed photonic crystals has utilized thermal sintering and etching of close packed colloidal crystals[40-42]. This work has also employed conformally backfilling[38, 43, 44] these close packed colloidal crystals. It should be noted that the resulting photonic crystal materials retain the disorder present in the original close packed crystals.

In the work here we demonstrate a straightforward method to form *non close-packed* highly ordered fcc direct and inverse opal silica photonic crystals materials. We show that size and charge polydispersity has surprisingly little impact on ordering for colloidal particle systems that are formed through electrostatic self assembly. Our group has utilized the high ordering of electrostatically self assembled crystalline colloidal array (CCA) photonic crystal materials since the mid-1980's[45-50]

More recently we polymerized a hydrogel around electrostatically self assembled CCA to form a polymerized CCA (PCCA). This PCCA is a responsive photonic crystal material[51] which proved useful for chemical sensing. [52-57], as well as for sensing temperature.[58, 59] We also developed magnetically responsive superparamagnetic and ferrimagnetic photonic crystal materials[60-62], as well as, photonic crystals that respond to light as optical switching materials. [63-67]

Electrostatic CCA self assembly relies on the electrostatic repulsions between colloidal particles of like charge. For the systems used here the colloidal particle surface groups are strong acid sulfonic acids which ionize in aqueous environments. For low ionic strength aqueous solutions the electrostatic interactions are large and occur over long distances (~1 μm) which enable formation of macroscopic fcc CCA crystals. The ordering appears superior to that which can occur for close packed crystals because the soft electrostatic potentials avoid glass formation,

they allow crystal annealing and they should ameliorate the disorder penalty for particle size and charge polydispersity.

Here we describe the fabrication of new highly ordered photonic crystal materials that utilize electrostatic CCA self assembly to form a highly ordered template. We then form a soft photonic crystal material where we lightly crosslink a hydrogel around the CCA template. We then condense solid silica within the PCCA hydrogel. This allows us to control the photonic crystal periodicity independently from the diameter of the colloidal particles making up the fcc crystal. This also allows us to tune the form of the dielectric constant modulation of the photonic crystal separate from its periodicity. We also demonstrate that we can remove the organic polymer and form an inverse opal structure. Thus, we can independently vary the periodicity and the silica wall thickness.

We show that our simple, electrostatic self assembly process gives rise to a photonic crystal with higher ordering compared to typical close-packed photonic crystal structure. We use DLVO theory to model interparticle interactions to gain insight into why electrostatic self assembly results in high order.

4.2   EXPERIMENTAL METHODS

4.2.1   Materials

2,2-diethoxyacetophenone (DEAP, 98%, Acros Organics), polyethylene glycol dimethacrylate 200 (Polysciences Inc.), 2-hydroxyethyl acrylate (98%, Polysciences Inc.), diethylene glycol (Sigma), anhydrous ethyl alcohol (Pharmco Inc.) and tetraethyl ortho silicate (TEOS, Fluka)

were used as received. Figure 1 shows our synthetic scheme for fabricating an inverted photonic

crystal (IPC) structure by using a CCA template.

CHARGED PS LATEX **CRYSTALLINE COLLOIDAL ARRAY (CCA)** **POLYMERIZED CRYSTALLINE COLLOIDAL ARRAY (PCCA)**

DIALYSIS

HEMA + PEG DMA

UV-PHOTO POLYMERIZATION

INFILTRATION OF SOL GEL PRECURSOR

450 °C

PCCA REMOVAL

150 °C

SOLVENT REMOVAL

INVERTED STRUCTURE **DRIED SIPCCA** **SILICA INFILTRATED PCCA)SIPCCA**
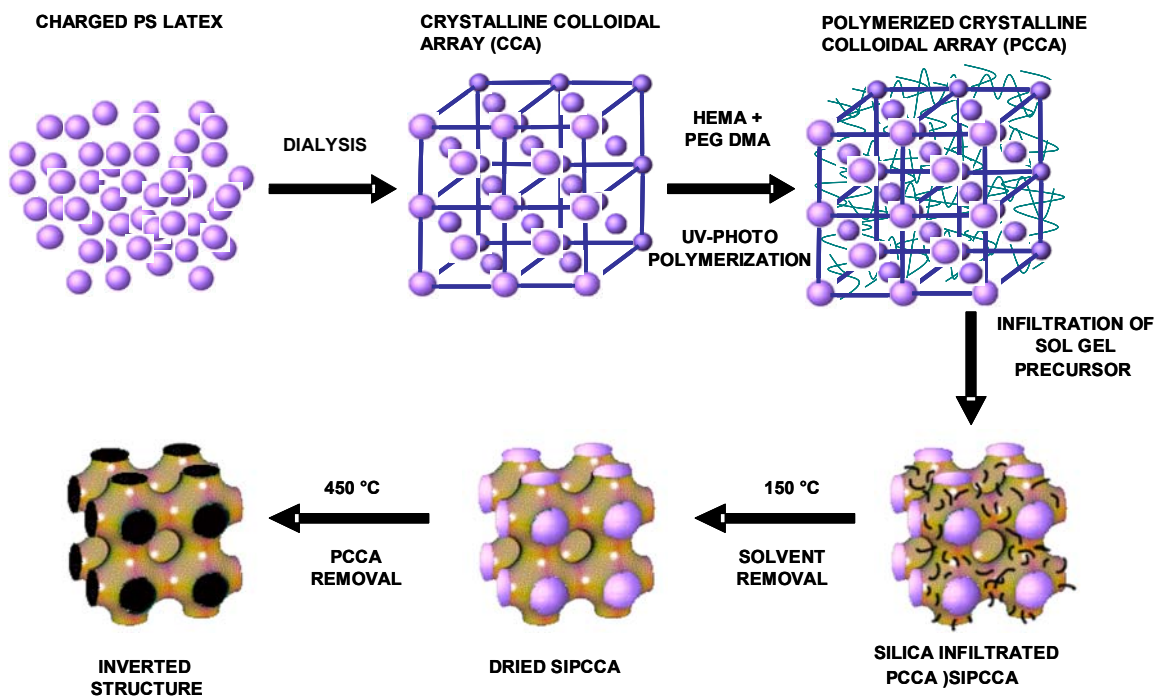
Figure 4-1 Charged polystyrene colloidal particles are dialyzed. Non ionic monomers are added. The

system electrostatically self assembles into an fcc CCA which is UV-photopolymerized to fabricate a PCCA. A

TEOS precursor is infiltrated into the hydrogel network and silica is condensed within the PCCA. The newly

formed siPCCA is then heat treated to remove solvent and organic polymer forming the inverted structure.

4.2.2 Preparation of PCCA

The highly-charged, non-cross-linked, monodisperse polystyrene colloids (Figure 1) used to

fabricate the siPCCA were prepared by emulsion polymerization.[68] The colloidal particle size as

measured by TEM is 180 nm ± 4nm. The colloidal particles were cleaned by dialysis against

deionized water followed by shaking with mixed bed ion-exchange resin (Bio-Rad AG501-X8

(D)) In a typical PCCA recipe 2,2-hydroxyethyl methacrylate (6 g, 4.6×10^{-2} mol, Polysciences) and polyethylene glycol dimethacrylate (0.174 g, 5.3×10^{-4} mol, Polysciences) were mixed together in a 2 dram vial. Aluminum oxide was added to remove the inhibitor contained in the monomer solutions. The solutions were centrifuged for 5 min to remove the aluminum oxide. 0.5 g of the deinhibited monomer solution supernatant was added to 2 g of the cleaned, highly charged colloidal particle dispersion.

The resulting mixture was shaken for 30 sec. 10% diethoxyacetophenone (DEAP; 10 μL, 3.84 μmol; Aldrich) was added to the mixture which was then vortexed for 30 sec. The mixture was injected between two quartz plates separated by a 125 μm Parafilm spacer. UV-photopolymerization was performed by using two UV mercury lamps (Black Ray) for 13 min. The PCCA film was removed from the quartz cell and equilibrated in a deionized water bath.

4.2.3 Infiltration of Sol-Gel precursor

A silica sol-gel precursor solution was prepared using a 1:1:3 molar ratio of TEOS/EtOH/water adjusted to a pH of 2 with concentrated HCl. The fabricated PCCA film template was immersed into two ml of the precursor solution.

Polymerization and condensation of the TEOS occurred around and within the PCCA hydrogel matrix over the course of 5 days, generating an alcogel within the PCCA template. The silica network was allowed to age and strengthen for an additional five days before further processing.

4.2.4 Solvent Removal

The silica sol-gel infiltrated PCCA was solvent-exchanged for one week in ethanol. This ethanol-containing, silica-infiltrated PCCA (siPCCA) was then heated at 85 °C for 1 day, followed by heating to 150 °C for 5 hrs to remove all solvent.

4.2.5 Polymer Removal

After solvent removal, the temperature was increased to 250 °C and held for 6 hours to melt the polystyrene colloidal particles as shown in Fig. 2. Higher temperature treatment at 450 °C removed all organic polymer materials, leaving behind only the infiltrated silica.[69] Upon firing the sample cracked into small fragments consisting of monoliths approximately 2 mm on a side.

4.2.6 Physical Measurements

Transmission electron microscopy was used to measure particle size. We used a Phillips FEG XL-30 FESEM operating in the ranges of 10-50 KeV to image the inverted structures. Diffraction spectra were obtained at room temperature using an Ocean Optics USB2000 spectrophotometer with a six-around-one reflectance probe. Solvent refractive indices were measured by using a Bausch & Lomb refractometer.

4.3   RESULTS AND DISCUSSION

4.3.1   Photonic Crystal Structure

Fig. 2 shows four positions on a cleaved (111) surface of a silica filled PCCA (siPCCA) sample at room temperature after heat treatments at 85 ºC, 150 ºC, 250 ºC, and 450 ºC. This siPCCA was formed as shown in Fig. 1 by polymerizing a hydrogel around a CCA, which self-assembled due to the electrostatic repulsions between colloidal particles. The CCA generally forms as a face centered cubic (fcc) lattice with a spacing determined by the particle number density.
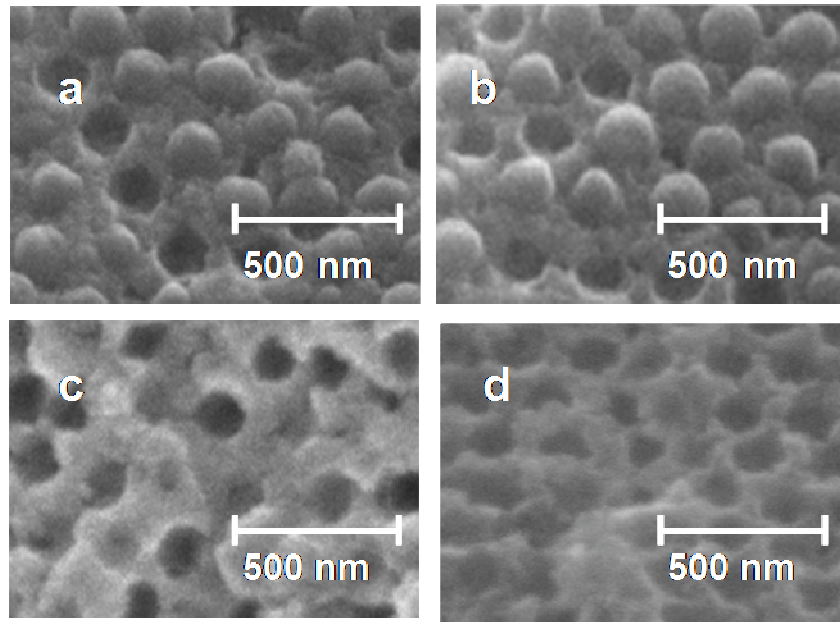
Figure 4-2 SEM images of a room temperature cleaved siPCCA showing its evolution through the heat treatment process. a. At 85 °C the colloidal particle lattice remains intact. b. After 150 °C heat treatment little deformation of polystyrene colloidal particles is evident. c. 250 °C heat treatment melts the colloidal particles leaving some polymer behind. d. The 450 °C heat treatment removes all of the organic polymer material leaving behind a highly ordered inverted opal of pure silica.

The hydrogel polymerizes around the fcc lattice without altering the CCA order. TEOS was then infiltrated and condensed into the PCCA. Figs. 2a and b show that the PCCA colloidal lattice remains intact upon condensation of silica within the PCCA hydrogel matrix. Some polystyrene particles have fallen out of the surface which proves that the PCCA hydrogel embeds the CCA lattice and does not covalently attach to the colloidal particles.

Figure 2c shows the siPCCA after heat treatment at 250 ºC, which exceeds the 240 ºC melting point of the non-cross-linked polystyrene[70]. The colloidal particles appear to have significantly melted, leaving holes in the surface. The siPCCA at this stage turned brown indicating that polymer degradation occurred. Energy dispersive x-ray analysis of the wall space shows both silicon and carbon peaks indicating the presence of both organic material and the infused silica.

Heat treatment at 450 ºC (Fig. 2d) removed the brown color of the siPCCA. Energy dispersive x-ray analysis shows the absence of a carbon peak in the wall space. The organic polymer material has burnt out during this heat treatment, leaving a pristine *non-close-packed* silica inverted opal structure. Thermogravimetric analysis shows a decreasing mass as the structure is heated from 150 ºC to 450 ºC. However, it was impossible to measure the relative organic polymer loss because of a pure silica coat of unknown thickness formed around the siPCCA during the condensation of the TEOS precursor solution within the PCCA.

Fig. 3 shows the SEM image of a different siPCCA sample, where a razor blade was used to abrade the (111) surface. We used these SEM images to determine the siPCCA in-plane spacing of the 85 ºC, 150 ºC, 250 ºC and 450 ºC heat-treated samples. These in plane spacings were used to calculate the fcc (111) lattice plane spacing, d_{111}:

$$d_{hkl} = \frac{\sqrt{2}D}{\sqrt{h^2 + k^2 + l^2}}$$

Equation 4-1

where D is the nearest neighbor spacing observed in the Fig. 2 SEM, and h, k, and l are the Miller indices of the presumed face-centered-cubic crystal.

Abrasion of the siPCCA sample removes the silica coat as well as latex spheres. The SEM derived (111) lattice plane spacing for the 85 °C and 150 °C heated samples were essentially identical at 245±4 nm and 245±4 nm (mean ± SD) which indicates no decrease in lattice constant upon heating. A slight decrease was calculated for the (111) lattice plane spacing for the 250 °C (238±4 nm) and 450 °C (224±5 nm) heat treated samples. The ordering and interparticle spacing which originated from the electrostatic formation of the original CCA lattice, which was rigidified by formation of the PCCA and was set by the silica condensation, is maintained throughout the heat treatment process.
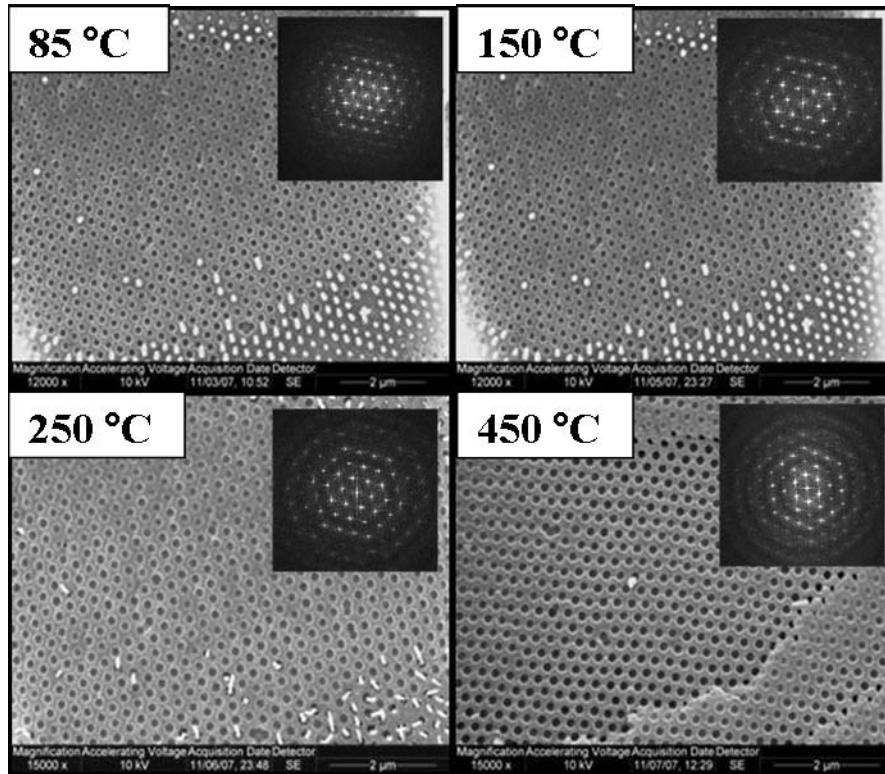
Figure 4-3 SEM images of the (111) plane obtained by abraiding the surface of the siPCCA. The 450 °C sample needed to be reabraided because the palladium sputter coating had fallen off. Insets: Fourier transforms show the high ordering within the (111) plane.

Figure 4 shows the room temperature spectrum of the 180° back diffracted light for light incident normal to the (111) surface of the heat treated siPCCA sample. The diffraction of the siPCCA blue-shifts as the treatment temperature increases above 150 ℃. Bragg's law (Eqn 2) indicates that at a constant incident glancing angle a decrease in diffraction wavelength requires a decrease in the average material refractive index, n_{avg}, or the d_{111} lattice plane spacing, or both.

$$m\lambda = 2d_{111}n_{avg}\sin\theta$$

Equation 4-2
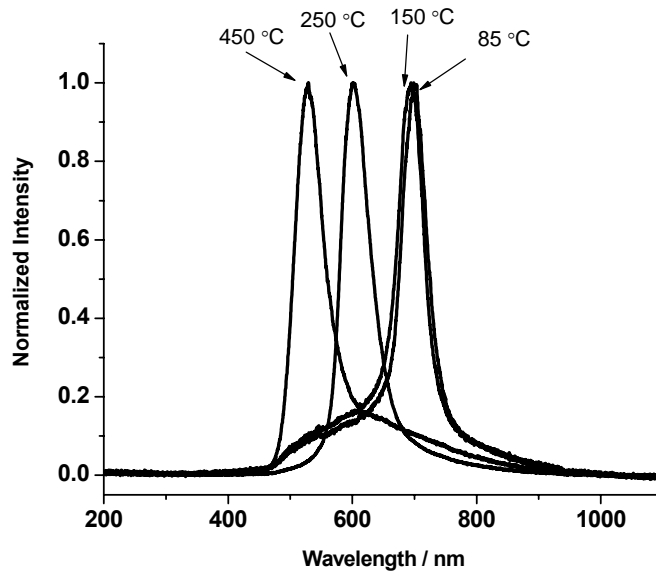
Figure 4-4 Room temperature diffraction spectra for light incident normal to the (111) planes of the siPCCA measured after heat treatments of 85, 150, 250 ºC, and 450 ºC. As discussed in the text, the blue-shift in diffraction is due to the refractive index decrease which results from the loss of polymeric material during the heat-treatment process

where m is the order of diffraction, λ is the diffracted wavelength in air and θ is the glancing angle of incidence. The average refractive index, n_{avg}, is approximately equal to the refractive indices of the components, n_i, weighted by their volume fractions, φ_i.

$$n_{avg} = \sum n_i \varphi_i$$

Equation 4-3

Substituting the SEM calculated d_{111} and the diffracted wavelength in Bragg's law we can calculate n_{avg} for each treated sample (Table 1). Clearly, the average refractive index decreases at heat treatments of greater than 150 ºC, indicating removal of the organic material.

Table 1 Increasing heat treatment temperatures vaporize the polymer decreasing n_{avg} and slightly decreasing the nearest neighbor spacing. Removal of the organic material increases the void space.

temp	n_{avg}	d_{111}	φ_{silica}	φ_{void}	$\varphi_{organic}$
85 °C	1.42	245	0.2	0.2	0.6
150 °C	1.42	245	0.2	0.2	0.6
250 °C	1.27	236	0.22	0.47	0.31
450 °C	1.12	224	0.26	0.74	0

At 450 ºC the inverted photonic crystal contains only silica and void space so that the relative volume fractions of each, φ_{silica} and φ_{void}, can be calculated from the values of n_{avg} and n_{silica}

$$n_{avg(450°C)} = \varphi_{silica} n_{silica} + \varphi_{void} n_{void}$$

Equation 4-4

The refractive index of silica in the inverted photonic crystal was determined by infusing solvents[71] into the 450 °C pure silica sample in order to refractive index match the silica which causes the diffraction to disappear (Fig. 5a). For this experiment, an inverted siPCCA was heat treated to 450 °C and the diffraction from a single region was monitored. We infused the solvents for 24 hrs to achieve equilibrium. The diffraction disappears upon infiltration of chloroform indicating that $n_{silica} \sim 1.45$, the refractive index of $CHCl_3$. Thus, using eqn 4, we calculate $\varphi_{silica} = 26\%$ for the 450 °C heat treated sample, giving a void volume fraction of $\varphi_{void} = 0.74$.
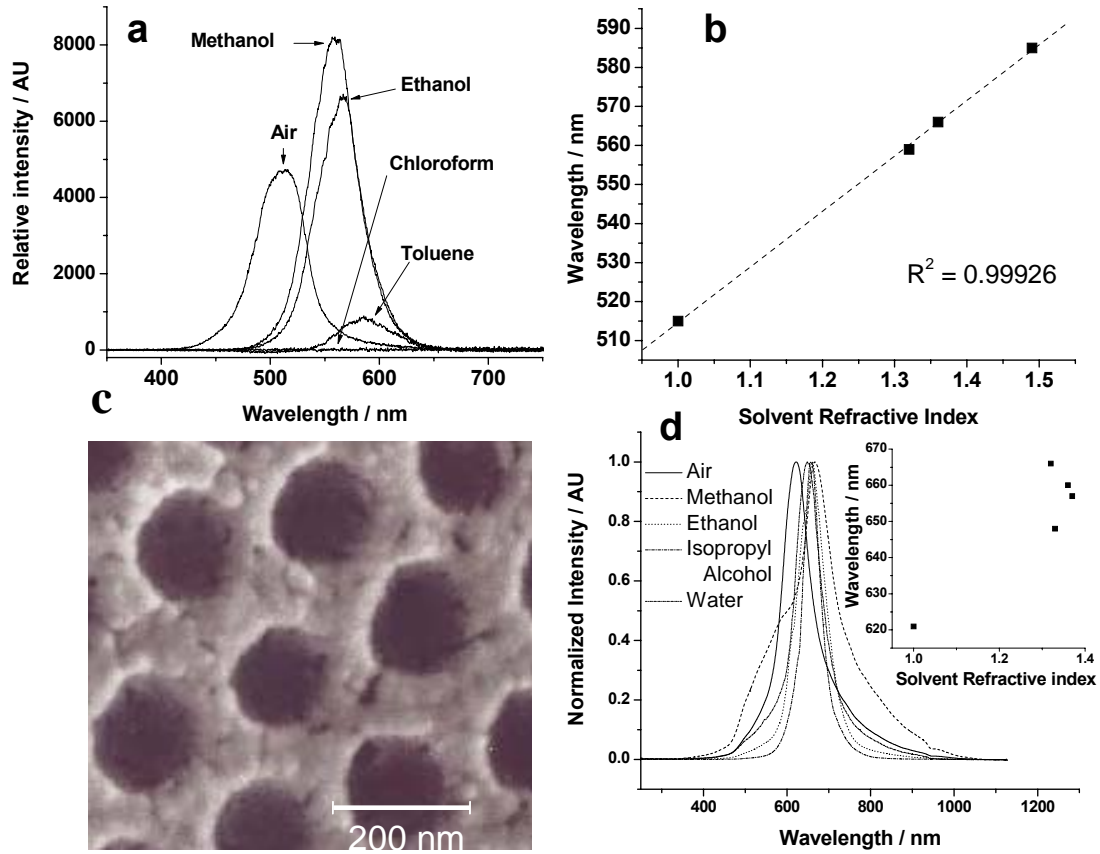
Figure 4-5 Study of void volume of siPCCA. a. Diffraction spectra obtained from the 450 °C heat treated siPCCA in air and with solvent infiltrations of methanol, ethanol, chloroform, and toluene. b. Linear best fit of the diffraction maxima of the 450 °C solvent infiltration data of a versus solvent refractive index. c. SEM image showing wall porosity of siPCCA after 450 °C heat treatment. d. Diffraction dependence on solvent refractive index for 250 °C heat treated sample.

Table 1 shows that n_{avg} decreases for the 250 °C sample, indicating loss of organic polymer. Given a constant φ_{silica} we can calculate the polymer and void volume fraction for all of the samples by using eqn 5.

$$n_{avg} = \varphi_{silica} n_{silica} + \varphi_{void} n_{void} + \varphi_{polymer} n_{polymer}$$

Equation 4-5

By assuming that the remaining polymer composition is identical to that of the original PCCA we can estimate a volume average polymer refractive index, $n_{polymer} \sim 1.55$. Table 1 shows that the 85 °C heat treated siPCCA has a $\phi_{polymer}=0.6$, which is ~50% greater than that of the originally prepared PCCA. This occurs because, although the original PCCA swells after exposure to the silica precursor solution, it then dramatically shrinks as the silica condenses within the PCCA.

Table 1 shows that there is no loss of polymer for the 150 °C heat treated sample, but almost half of the polymer is lost for the 250 °C heat treated sample. We calculate that the void volume fraction of 20 % of the 85 and 150 °C heat treated samples almost doubles for the 250 °C heat treated sample. The void volume fraction maximizes at 74% for the 250 °C heat treated sample. It should be noted that we find a 20 % void volume fraction for the 85 °C heat treated sample that results from evaporation of the solvent in the original silica condensed siPCCA. The increased silica volume fraction for the 250 °C heat treated sample results from the volume decrease of the siPCCA evident from the observed SEM decreased in-plane spacing as discussed above. Our calculations of the volume fractions at the lower heat treatment temperatures took cognizance of the calculated decrease in the (111) lattice plane spacing calculated from the SEM data. We account for the change in silica volume fraction through the proportionality $\varphi_{silica}V = \varphi'_{silica}V'$, where V is the original siPCCA volume and φ'_{silica} and V' are the silica volume fraction and unit cell volume after heat treatment.

We can independently determine ϕ_{silica} at 450 ºC from a plot of the dependence of the diffraction wavelength for normal incidence upon the refractive index of the infiltrated solvent (Fig. 5b). The slope of eqn 6 can be used to calculate ϕ_{void} and the intercept to calculate ϕ_{silica}.

$$\lambda = 2d_{111}n_{silica}\varphi_{silica} + 2d_{111}n_{solvent}\varphi_{void}$$

Equation 4-6

Utilizing the derived (111) lattice plane spacing and the slope we determined a silica filling fraction of φ_{silica} = 17%, indicating a lower φ_{silica} than calculated from the excellent assumption that the diffraction wavelength in air can be simply related to the average siPCCA refractive index given the SEM determined lattice spacing.

We conclude that the decreased slope calculated from eqn 6 results from sealed voids which are inaccessible to the solvent. The SEM in Fig 5c shows the complex morphology of the walls of the siPCCA. Obviously, the silica has condensed as particles which are closely packed. It would not be surprising that part of the voids would be sealed off from solvent infiltration.

To calculate the void volume inaccessible to solvent we can rewrite eqn 6 as:

$$\lambda = 2d_{111}n_{silica}\varphi_{silica} + 2d_{111}n_{solvent}\varphi_{accvoid} + 2d_{111}n_{air}\varphi_{inaccvoid}$$

Equation 4-7

where the total void volume is partitioned into inaccessible and accessible voids. From this expression we calculate a 9% unfillable void space located in the silica wall space giving the silica wall a ~35% porosity.

Figure 5d shows the results of solvent infiltrations into the 250 °C heat treated siPCCA where some, but not all, of the polymer was removed. The diffraction spectrum in air is broad and not symmetric and shows shoulders on both sides indicating a relatively inhomogeneous siPCCA, in contrast to that of the Fig. 5a 450 °C heat treated siPCCA. Infiltration of methanol results in a very complex bandshape indicating a variable accessibility into this siPCCA. In contrast, the bandshapes of the ethanol, isopropanol and water infiltrations

81

are more symmetric which indicates a chemical selectivity for solvent accessibility in the presence of organic polymers. Peculiarly, the largest red-shift in diffraction results from methanol (shoulder), which has the lowest refractive index. Obviously, there is some interesting interfacial chemical selectivity present.

4.3.2 Wall Spacing and Periodicity of siPCCA, Surface Morphology

The use of CCA electrostatic self-assembly enables the fabrication of fcc photonic crystal materials where the nearest neighbor spacing can be defined independently of the interparticle spacing. For inverse opal fcc crystals this allows us to independently control the fcc sphere void spacing and the wall thickness as shown in Fig. 6a and b which show two different siPCCA's made from identical colloidal particles, but where the lattice constant is varied by changing the CCA particle number density. The decreased particle number density increases the wall thickness and the silica wall volume fraction.
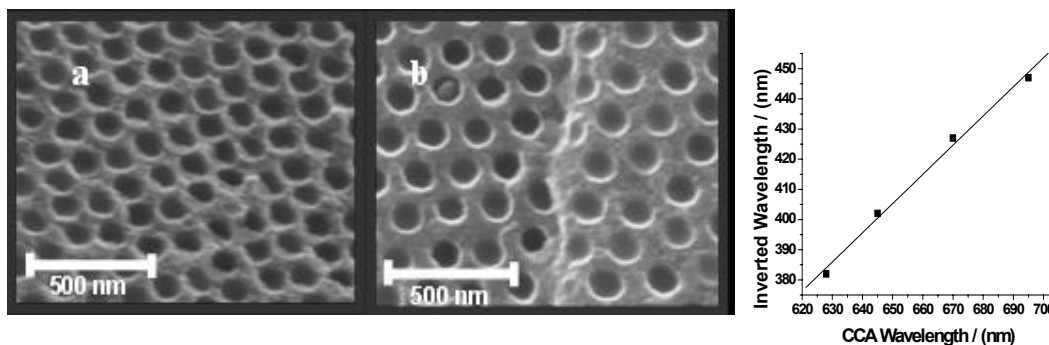
Figure 4-6 (a) SEM of 450 °C heat treated siPCCA prepared from 186 nm diameter 18 wt% CCA $(1.5 \times 10^{14}$ particles/cm^3) and (b) 12 wt% CCA $(9.9 \times 10^{13}$ particles/cm^3) CCA A smaller particle number density increases the nearest-neighbor spacing. (c) Linear correlation between CCA diffraction and diffraction of 450 °C heat treated siPCCA.

Figure 6c, which demonstrates proportionality between the CCA diffraction and that of the 450 °C heat treated siPCCA demonstrates that the original template CCA determines the inverted siPCCA structure and spacing. In summary, the results above demonstrate that we have developed a simple scalable, inexpensive process to create highly ordered photonic crystal materials. We use electrostatically stabilized CCA as a template to form highly ordered siPCCA and inverse opal silica photonic crystals, where the spacing and wall thickness can be independently varied.
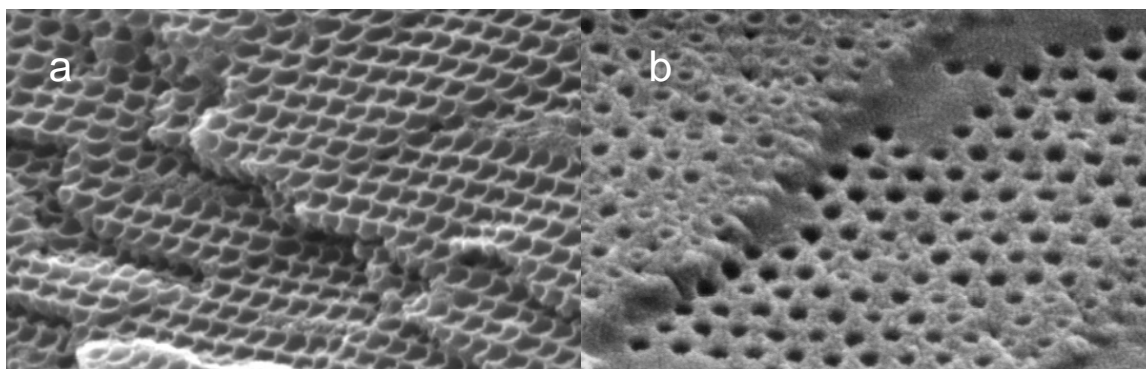
Figure 4-7 SEM measured at a 50° angle to a 450 °C heat treated cleaved siPCCA formed with a. 1.5×10^{14} particles/cm^3 and b. 9.9×10^{13} particles/cm^3 particle number densities. The high particle number density siPCCA wall morphology shows clear ridges between nearest neighbors. The siPCCA made with low particle number density show smooth plateau regions between sphere holes.

The Fig. 7 SEM of inverted siPCCA inverse opal samples at high and low particle density show clear differences in morphology of the cleaved surfaces. In contrast to the low particle density surface which has plateaus between holes, the high particle number density surface shows ridges between the originally close packed particles giving a hexagonal array of bowl shaped cavities which may prove useful for future applications.

4.3.3 Ordering

As shown in the SEM photographs above and in Fig. 8 the siPCCA and the inverse opal photonic crystal materials are highly ordered over long ranges. Fig. 8 shows an siPCCA cleaved mainly along the 100 plane surfaces. The ordering of the SEM visually suggests high order, possibly higher than that of the more typically studied close packed photonic crystal materials made from colloidal particles with similar particle size monodispersities.
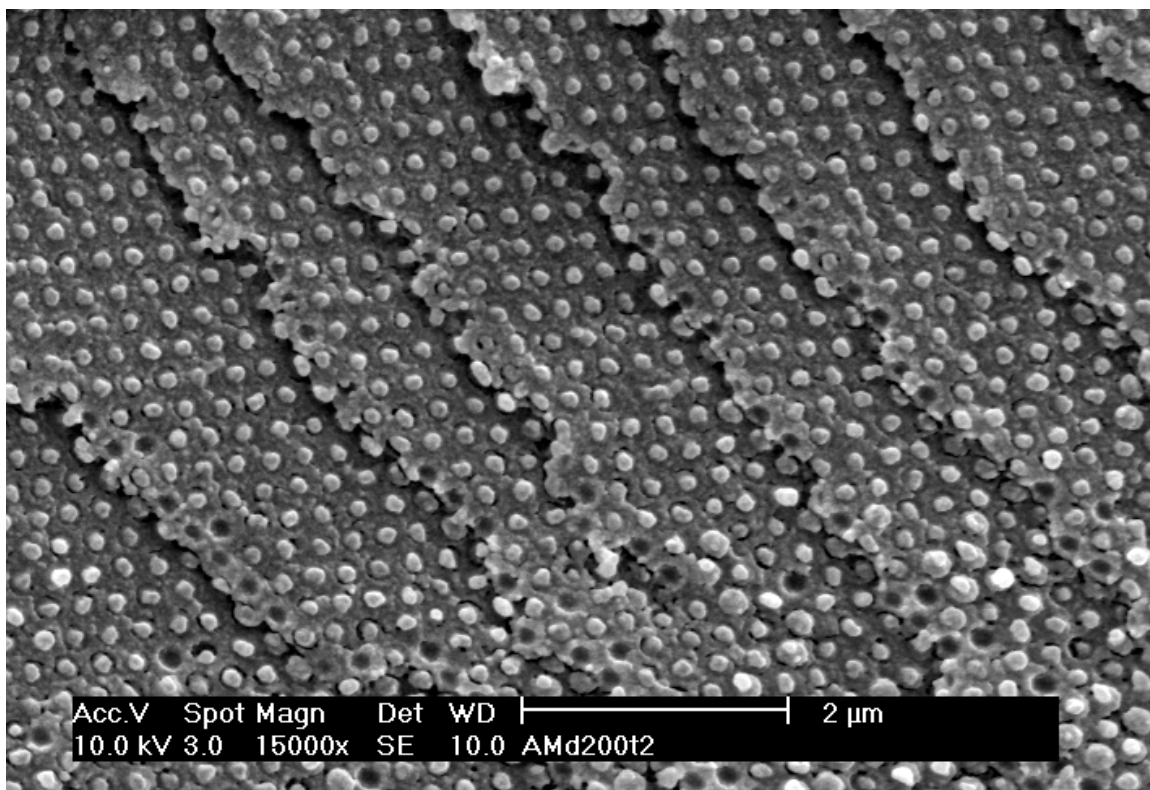
Figure 4-8 SEM of cleaved cross-section of low particle density siPCCA showing exposed (100) planes.

The presumed increased ordering of the siPCCA compared to close packed photonic crystals is expected from the superior ordering of the original CCA template. The ordering of the CCA derives from soft electrostatic repulsions between colloidal particles. Because of the

soft repulsive interactions, colloidal particle polydispersity should have less impact on the ordering of electrostatically stabilized CCA than would occur for hard sphere-interacting close packed systems, as shown below.

This phenomenon is evident from Fig. 9 which shows the disorder induced by the inclusions of ~4-fold and ~2-fold larger particles in the original CCA template. The deformation in the crystal lattice anneals out within approximately two particle layers, due to the CCA soft electrostatic interparticle potential.
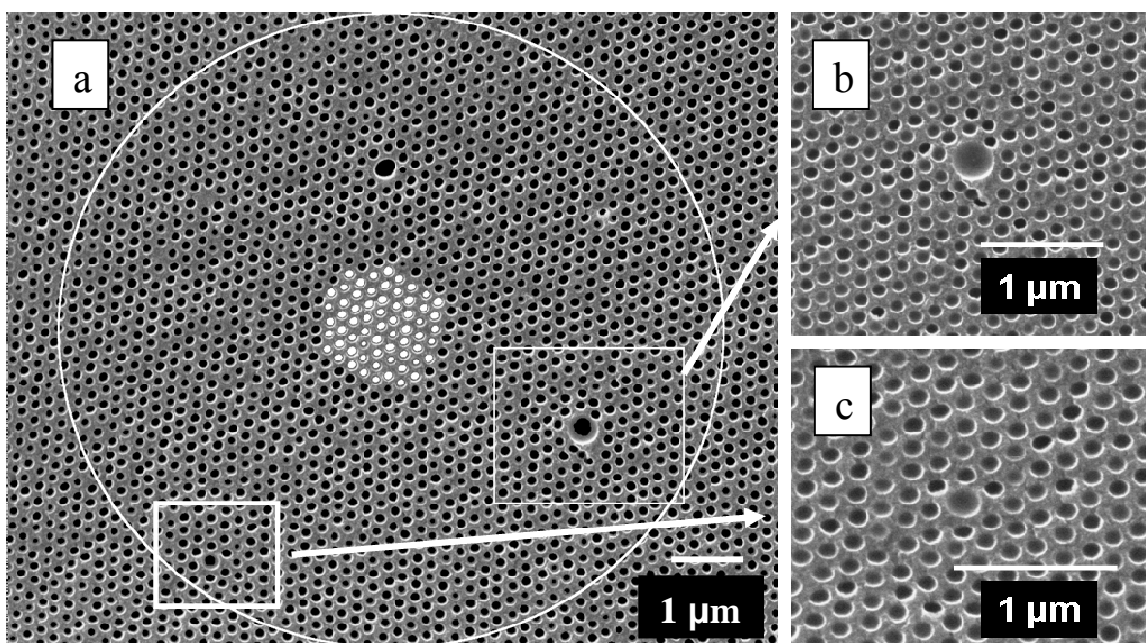
Figure 4-9 (a) SEM image showing the (111) plane surface of a silica inverse opal photonic crystal which was heat treated to 450 °C. The white circle encloses the area used to calculate the pair correlation function (PCF). The small white circles at the center of the image shows the different origins used for the PCF. (b) Expanded images showing impact of a 4-fold and (c) 2-fold larger colloidal particles on the ordering. The strains in the periodic order of the lattice anneal over approximately two particles layers.

To quantitatively analyze the Fig. 9a ordering of our inverse opal siPCCA we calculated the two dimensional pair correlation function (PCF), g(r) of the area enclosed by the white circle

$$g(r) = \frac{1}{\langle \rho \rangle} \frac{dn(r, r+dr)}{da(r, r+dr)} .$$

Equation 4-8

We calculated the number of spheres, *dn*, which lie at a radius of r from the defined origin within a circular ring of width *dr*. As r increases g(r) probes the long range particle ordering within the (111) plane. We repeated this calculation for multiple origins within the lattice (white colored centers). The average of the g(r) values was normalized by the average particle number density and the area of the circular ring $da=2\pi r dr$.
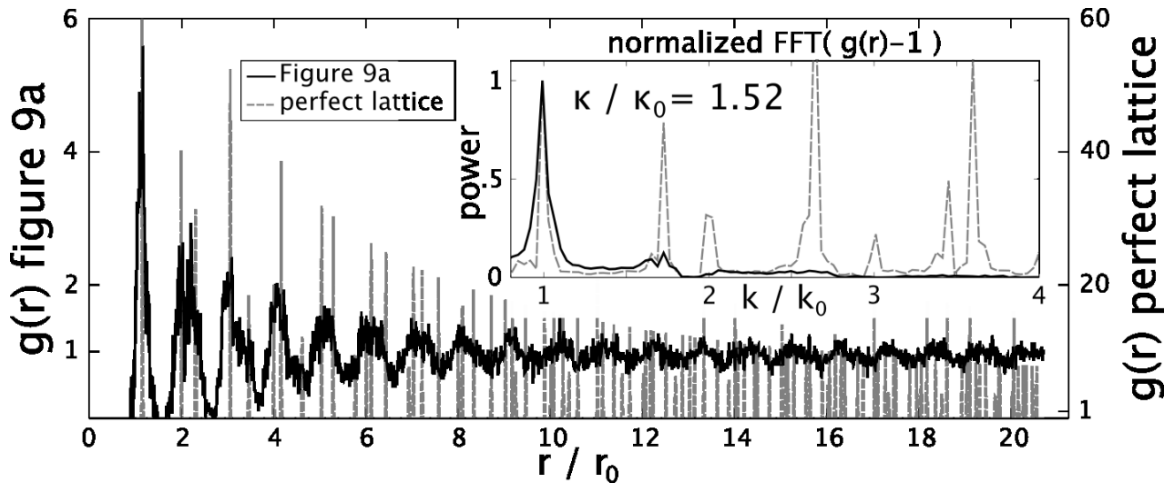
Figure 4-10 Calculated pair correlation function (PCF) from sample shown in Fig. 9a and PCF for a perfect lattice (vertical dashed lines) as a function of r/r_o, where r_o is the mean near neighbor center to center spacing. The inset shows the Fourier Transforms (FT) of both PCF where the dotted lines show the FT of the perfect lattice.

For well ordered crystals g(r) will be large for r values corresponding to multiples of the in-plane (111) lattice constants. In contrast, g(r) will be small for intermediate r values. Colvin

et al recently showed highly ordered photonic crystal lattices generate g(r) showing many peaks over large values of r which clearly indicate good long range ordering.[34]

A quantitative measure of ordering is obtained from the ratio of the Full Width at Half Maximum (FWHM) of the first peak in the Fourier Transform (FT) of the function g(r)-1 of the SEM image, κ, to that of a perfect lattice, κ_o, with the same number of lattice points (see Fig. 10 inset). $\kappa/\kappa_o = 1$ will occur for a perfect 2-D crystal, whereas $\kappa/\kappa_o \leq 1.5$ suggests very highly ordered photonic crystal surfaces.[34]

We can qualitatively understand the decreased impact of particle polydispersity on CCA ordering compared to that of close-packed particles by examining the interparticle repulsive interactions. At present the electrostatic interaction between charged particles is modeled by using DLVO theory.[72] We are aware that this is only a rough approximation since it is well known that DLVO theory fails to describe particle repulsion for particles with high charge.[73] Further the effective particle charge must be renormalized to significantly decrease the charge density so that DLVO theory can successfully model electrostatic interactions for real colloidal dispersions.[74]

The DLVO interaction potential, $U_{DLVO}(r)$ between particles with different sizes and charges is:

$$U_{DLVO}(r) = \frac{Z^*_1 Z^*_2 e^2}{\varepsilon} \left[\frac{e^{\kappa a_1}}{1 + \kappa a_1} \right] \left[\frac{e^{\kappa a_2}}{1 + \kappa a_2} \right] \frac{e^{-\kappa r}}{r}$$

Equation 4-9

where Z^*_1 and Z^*_2 are the renormalized charges on two particles of radius a_1 and a_2. e is the fundamental electronic charge, ε is the static dielectric constant of the medium and r is the interparticle separation distance.[75] The Debye length, $1/\kappa$, is given by

$$1/\kappa = \sqrt{\frac{4\pi e^2}{\varepsilon k_B T}\left[n_p Z^* + n_i\right]}$$

Equation 4-10

where k_B is Boltzmann's constant, n_p is the particle number density and n_i is the ionic impurity concentration. We presume that the system contains no added impurities, so that $n_i = 0$. For the discussion below we assume that a 10% variation in a single particle diameter and/or single particle charge results in a negligible change in the Debye length of the system.
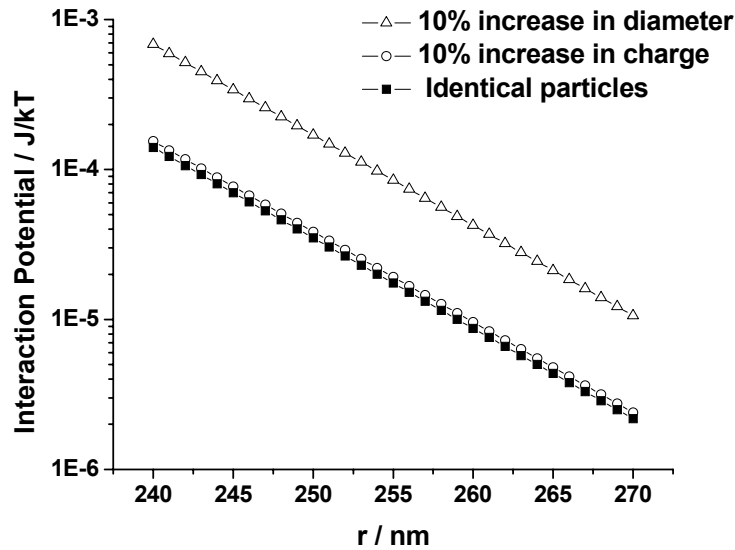
Figure 4-11 Dependence of $U_{DLVO}(r)$ upon interparticle distance between (■) two identical particles of 130 nm diameter with a renormalized charge of 1000; (○) between two identical particles of diameter 130 nm, where one particle has a renormalized charge of 1000 and the other 1100; (△) between a particle of diameter 130 nm and one 10% larger, both with a renormalized charge of 1000.

The discussion below assumes a nominal colloidal particle diameter of 130 nm and a renormalized charge of Z=1000. This charge renormalization corrects for extra charge screening not included in DLVO theory. We choose for discussion a CCA nearest neighbor distance of 250 nm between particles, giving a particle number density of 1.613×10^{14} particles/cm^3. We calculate $1/\kappa$ for our system to be 10.4 nm.

Fig. 11 shows that for this distance separation there is a negligible difference in the DLVO potential in response to a 10 % increase in particle charge. Thus, changes in particle charge must negligibly impact the CCA ordering at these nearest-neighbor distances.
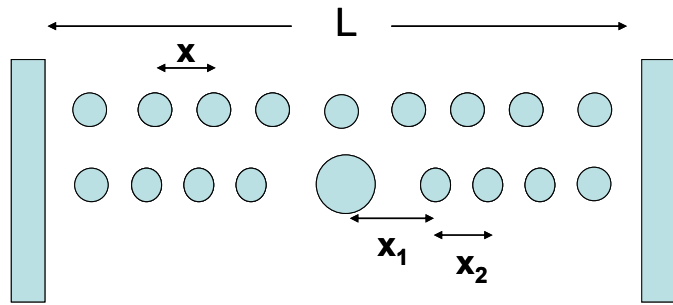
In contrast, Fig. 11 shows that DLVO theory predicts a ~10 % increase in repulsive interactions with a 10 % increase in the particle diameter. However, the potential

Figure 4-12 Model for response of one dimensional array of N particles to a single defect particle of increased diameter. The N particles are arrayed along a cell of length L. In the top array the particle diameters are identical and the system self assembles such that the spacings between particles are identical at $x = L / (N +1)$. In the bottom array one particle is replaced with a particle of larger diameter. The distance between the larger diameter particle and the adjacent particle is $x_1 = x + \delta$, while the distance between the other identical particles is $x_2 = L-2x_1 / (N-1)$. δ is determined by the equilibrium between forces.

energy difference at the same interparticle spacing of 250 nm is quite small, ~2 x 10^{-3} k$_B$T per particle.

This soft electrostatic repulsive potential prevents defect particles from significantly impacting CCA ordering. We can roughly model the change which occurs in the interparticle spacing brought on by a single defect particle with a 10 % increased particle diameter by modeling the forces in a one dimensional array of particles that spans the characteristic photonic crystal macroscopic size (Fig. 12). We calculate the forces between particles, neglecting all but nearest neighbor interactions, from the derivative of the DLVO potential with respect to interparticle distance, r.

$$F(r) = \frac{-Z_1 e \cdot Z_2 e}{\varepsilon} \left[\frac{e^{\kappa a_1}}{1 + \kappa a_1} \right] \left[\frac{e^{\kappa a_2}}{1 + \kappa a_2} \right] \left[\frac{1 + \kappa r}{r^2} \right] e^{-kr}$$

Equation 4-11

We assume a linear array of N particles. We compare the distance between particles for an array of N identical particles   which is x= L/ (N+1). When a single particle is replaced with a defect particle having a 10% increase in diameter the particles expand around the defect particle and contract around the other particles until the forces balance.   This would result in a negligible average particle spacing decrease for the other particles since this spacing difference would be distributed over the other particles in the array.

We can look at this issue more quantitatively by equilibrating the forces between particles. Equations 12 and 13 show that $F(x_1)$ defines the force between the defect particle and its nearest neighbor while $F(x_2)$ defines the force between the remaining identical particles. We assume that the length of the particle array is constant at 250 μm

$$F(x_1) = \frac{-(Z_1 \cdot e)^2}{\varepsilon} \left[\frac{e^{\kappa \alpha_1}}{1 + \kappa \alpha_1} \right] \left[\frac{e^{\kappa \alpha_2}}{1 + \kappa \alpha_2} \right] \left[\frac{1 + \kappa x_1}{x_1^2} \right] e^{-\kappa x_1}$$

Equation 4-12

90

$$F(x_2) = \frac{-(Z_1 \cdot e)^2}{\varepsilon} \left[\frac{e^{\kappa\alpha_1}}{1 + \kappa\alpha_1} \right] \left[\frac{e^{\kappa\alpha_1}}{1 + \kappa\alpha_1} \right] \left[\frac{1 + \kappa x_2}{x_2^2} \right] e^{-\kappa x_2}$$

Equation 4-13

which represents the smallest dimension common to our CCA films. The nearest neighbor

spacing of this system before the addition of a particle defect is $x = 250$ nm. Therefore $N = 999$

particles.

Addition of a 10% increased particle diameter to the array changes the spacing between

the defect and its nearest neighbor to $x_1 = x + \delta$, where δ is the added spacing gained by the

equilibration of force between the defect and its nearest neighbor in equation 14,

$$x_2 = \frac{L - 2(x + \delta)}{N - 1}$$

Equation 4-14

By equilibrating the forces in eqn 12 and 13 we calculate $\delta = 5.7$ nm for a 10% increased

particle size. The separation between all other particles is very small:

$$x_2 = \frac{L - 2(x + \delta)}{N - 1} = \frac{x \cdot (N + 1) - 2x - 2\delta}{N - 1} = \frac{x(N - 1) - 2\delta}{N - 1} = x - \frac{2\delta}{N - 1}$$

Equation 4-15

For the typical large values of N there is negligible change in the interparticle spacings x_2

except exactly around the defect particle. In contrast for a close-packed system, a 10% change in

particle size generates a 10 % change in local spacing which disorders the system locally over

the distance that dislocations continue to disorder the system macroscopically.

4.4 CONCLUSIONS

We developed a simple, straightforward method to form *non close-packed* ultra-highly ordered fcc direct and inverse opal silica photonic crystals. We utilize a self assembled electrostatically stabilized crystalline colloidal array (CCA) template prepared from monodisperse, highly charged polystyrene colloidal particles. We then polymerize a hydrogel around the CCA (PCCA) and then condense silica within the PCCA to form a highly ordered siPCCA photonic crystal. Heating at 450 ℃ removes the organic polymer leaving the inverse opal structure.

This approach allows us to independently control the photonic crystal periodicity and size of the basis of the fcc unit cell. We select the fcc lattice constant by defining the particle number density of this electrostatically self assembled structure. Thus, we independently control the spacing between particles. The particle diameter used determines the wall spacing of the inverse opal photonic crystal and determines the shape of the photonic crystal dielectric constant modulation. This allows us to optimize the diffraction of our photonic crystal structures.

These fcc photonic crystals simply and spontaneously self assemble due to their soft electrostatic repulsion potentials. They show ordering as good or possibly better than close-packed photonic crystals formed by convective assembly. We show that colloidal particle size polydispersity has less impact on photonic crystal electrostatic ordering than occurs for ordering of close-packed crystals. Point defect induced crystal strains in electrostatically stabilized CCA anneal within ~two particle layers. We also show that charge polydispersity has only a small impact on crystal ordering and that the strains due to defect particles of different charge also anneal out over ~two particle layers.

4.5 AKNOWLEDGMENTS

4.6 REFERENCES

(1)   S. John, Phys. Rev. Lett. **1987**, 58 2486.

(2)   E. Yablonovitch, Journal de Physique, Colloque **1987**, C5 C5.

(3)   J. D. Joannopoulos, R. D. Meade, J. N. Winn, et al., *Photonic Crystals: Molding the Flow of Light*, 1995).

(4)   J. D. Joannopoulos, P. R. Villeneuve, and S. Fan, Nature (London) **1997**, 386 143.

(5)   M. Imada, L. H. Lee, M. Okano, et al., Applied Physics Letters **2006**, 88 171107/1.

(6)   D. J. Norris, Nature Materials **2007**, 6 177.

(7)   H. Takeda, A. Chutinan, and S. John, Physical Review B: Condensed Matter and Materials Physics **2006**, 74 195116/1.

(8)   C. Lopez, Advanced Materials (Weinheim, Germany) **2003**, 15 1679.

(9)   A. Arsenault, S. Fournier-Bidoz, B. Hatton, et al., Journal of Materials Chemistry **2004**, 14 781.

(10)   S. Noda, K. Tomoda, N. Yamamoto, et al., Science (Washington, D. C.) **2000**, 289 604.

(11)   A. Blanco, E. Chomski, S. Grabtchak, et al., Nature (London) **2000**, 405 437.

(12)   S. Noda, M. Fujita, and T. Asano, Nature Photonics **2007**, 1 449.

(13)   C. C. Cheng and A. Scherer, J. Vac. Sci. Technol., B: Microelectron. Nanometer **1995**, 13 2696.

(14)   T. Krauss, Y. P. Song, S. Thoms, et al., Electronics Letters **1994**, 30 1444.

(15)   O. Painter, R. K. Lee, A. Scherer, et al., Science (Washington, D. C.) **1999**, 284 1819.

(16)   E. Chow, S. Y. Liu, S. G. Johnson, et al., Nature (London) **2000**, 407 983.

(17)   B.-S. Song, S. Noda, T. Asano, et al., Nature Materials **2005**, 4 207.

(18)   Y. Akahane, T. Asano, B.-S. Song, et al., Nature (London) **2003**, 425 944.

(19)   M. Imada, A. Chutinan, S. Noda, et al., Phys. Rev. B **2002**, 65 195306/1.

(20)   D. N. Christodoulides, F. Lederer, and Y. Silberberg, Nature (London) **2003**, 424 817.

(21)   A. Chutinan, S. John, and O. Toader, Phys. Rev. Lett. **2003**, 90 123901.

(22)   J. V. Sanders, Nature (London) **1964**, 204 1151.

(23)   K. E. Davis, W. B. Russel, and W. J. Glantschnig, J. Chem. Soc. **1991**, 87 411.

(24)   H. Miguez, C. Lopez, F. Meseguer, et al., Appl. Phys. Lett. **1997**, 71 1148.

(25)   A. Van Blaaderen and P. Wiltzius, Advanced Materials (Weinheim, Germany) **1997**, 9 833.

(26)   P. Jiang, J. F. Bertone, K. S. Hwang, et al., Chem. Mater. **1999**, 11 2132.

(27)   Y. A. Vlasov, X. Z. Bo, J. C. Sturm, et al., Nature FIELD Full Journal Title:Nature **2001**, 414 289.

(28)   V. Kitaev and G. A. Ozin, Advanced Materials (Weinheim, Germany) **2003**, 15 75.

(29)   Z. Zheng, X. Liu, Y. Luo, et al., Appl. Phys. Lett. **2007**, 90 051910/1.

(30)   Y. Xia, B. Gates, Y. Yin, et al., Adv. Mater. (Weinheim, Germany) **2000**, 12 693.

(31)   Y. K. Koh and C. C. Wong, Langmuir **2006**, 22 897.

(32)   E. B. Sirota, H. D. Ou-Yang, S. K. Sinha, et al., Physical Review Letters **1989**, 62 1524.

(33)   J. P. Hoogenboom, D. Derks, P. Vergeer, et al., Journal of Chemical Physics **2002**, 117 11320.

(34)   R. Rengarajan, D. Mittleman, C. Rich, et al., Physical Review E: Statistical, Nonlinear, and Soft Matter Physics **2005**, 71 016615/1.

(35)   Z.-Y. Li and Z.-Q. Zhang, Physical Review B: Condensed Matter and Materials Physics **2000**, 62 1516.

(36)   A. Tikhonov, R. D. Coalson, and A. Asher Sanford, Phys Rev B **2007**, *Submitted*.

(37) K. Busch and S. John, Phys. Rev. E **1998**, 58 3896.

(38) E. Graugnard, J. S. King, D. P. Gaillot, et al., Advanced Functional Materials **2006**, 16 1187.

(39) M. Doosje, B. J. Hoenders, and J. Knoester, Journal of the Optical Society of America B: Optical Physics **2000**, 17 600.

(40) F. Meseguer and R. Fenollosa, Journal of Materials Chemistry **2005**, 15 4577.

(41) F. Meseguer, Colloids and Surfaces, A: Physicochemical and Engineering Aspects **2005**, 270-271 1.

(42) R. Fenollosa and F. Meseguer, Advanced Materials (Weinheim, Germany) **2003**, 15 1282.

(43) H. Miguez, N. Tetreault, S. M. Yang, et al., Advanced Materials (Weinheim, Germany) **2003**, 15 597.

(44) J. S. King, D. P. Gaillot, E. Graugnard, et al., Advanced Materials (Weinheim, Germany) **2006**, 18 1063.

(45) P. L. Flaugh, S. E. O'Donnell, and S. A. Asher, Appl. Spectrosc. **1984**, 38 847.

(46) R. J. Carlson and S. A. Asher, Applied Spectroscopy **1984**, 38 297.

(47) S. A. Asher, US Patent # 4,627,689 **1986**.

(48) S. A. Asher, P. L. Flaugh, and G. Washinger, Spectroscopy (Duluth, MN, United States) **1986**, 1 26.

(49) S. A. Asher, US Patent # 4,632,517 **1986**.

(50) S. A. Asher, U.S. Patent # 5,281,370 **1994**.

(51) S. A. Asher, J. Holtz, L. Liu, et al., J. Am. Chem. Soc. **1994**, 116 4997.

(52) J. H. Holtz and S. A. Asher, Nature (London) **1997**, 389 829.

(53) C. E. Reese, M. E. Baltusavich, J. P. Keim, et al., Analytical Chemistry **2001**, 73 5038.

(54) C. Sharma Anjal, T. Jana, R. Kesavamoorthy, et al., J. Am. Chem. Soc. **2004**, 126 2971.

(55) J. P. Walker and S. A. Asher, Anal. Chem. **2005**, 77 1596.

(56) K. W. Kimble, J. P. Walker, D. N. Finegold, et al., Anal. Bioanal. Chem. **2006**, 385 678.

(57) X. Xu, A. V. Goponenko, and S. A. Asher, Journal of the American Chemical Society **2008**, 130 3113.

(58)   J. M. Weissman, H. B. Sunkara, A. S. Tse, et al., Science (Washington, D. C.) **1996**, 274 959.

(59)   C. E. Reese, A. V. Mikhonin, M. Kamenjicki, et al., Journal of the American Chemical Society **2004**, 126 1493.

(60)   X. Xu, S. A. Majetich, and S. A. Asher, J. Am. Chem. Soc. **2002**, 124 13864.

(61)   X. Xu, G. Friedman, K. D. Humfeld, et al., Advanced Materials (Weinheim, Germany) **2001**, 13 1681.

(62)   X. Xu, G. Friedman, K. D. Humfeld, et al., Chem. Mater. **2002**, 14 1249.

(63)   M. K. Maurer, I. K. Lednev, and S. A. Asher, Advanced Functional Materials **2005**, 15 1401.

(64)   G. Pan, R. Kesavamoorthy, and S. A. Asher, Journal of the American Chemical Society **1998**, 120 6525.

(65)   G. Pan, R. Kesavamoorthy, and S. A. Asher, Phys. Rev. Lett. **1997**, 78 3860.

(66)   S. A. Asher, U.S. Patent # 5,452,123 **1995**.

(67)   R. Kesavamoorthy, M. S. Super, and S. A. Asher, Journal of Applied Physics **1992**, 71 1116.

(68)   C. E. Reese, C. D. Guerrero, J. M. Weissman, et al., J. Colloid Interface Sci. **2000**, 232 76.

(69)   T. Sen, G. J. T. Tiddy, J. L. Casci, et al., Angew. Chem., Int. Ed. FIELD Full Journal Title:Angewandte Chemie, International Edition **2003**, 42 4649.

(70)   J. A. Dean and Editor, *Lange's Handbook of Chemistry. 11th ed*, 1973).

(71)   C. F. Blanford, R. C. Schroden, M. Al-Daous, et al., Adv. Mat. **2001**, 13 26.

(72)   L. Belloni, Journal of Physics: Condensed Matter **2000**, 12 R549.

(73)   A. Naji, S. Jungblut, A. G. Moreira, et al., Los Alamos National Laboratory, Preprint Archive, Condensed Matter **2005** 1.

(74)   S. Alexander, P. M. Chaikin, P. Grant, et al., J. Chem. Phys. **1984**, 80 5776.

(75)   J. C. Crocker and D. G. Grier, Phys. Rev. Lett. **1996**, 77 1897.

5.0   SUMMARY OF WORK

We developed new insights into the CCA kinetics and degree of ordering. We enhanced the understanding of photon propagation in photonic crystal materials unraveling a decade long mystery of anomalous peaks in angularly resolved specular reflection measurements. These strides in photonic crystal research lay the ground work for improvements in CCA fabrication and their uses in novel optical devices. We developed a highly ordered non-close-packed inverted photonic crystal material from a non-close-packed CCA template. This new fabrication technique has expanded the use of CCA and PCCA materials, capturing their highly periodic structure for optical devices which can be utilized in harsh environments without the need of hydration to maintain crystal ordering.

In Chapter 2 we demonstrated the capability to understand and control the ordering of CCA photonic crystals. We showed the ability to follow, in real time, the crystallization process of a CCA by utilizing information obtained from time resolved Bragg diffraction interference fringe patterns. This important finding is crucial towards the understanding and improvement of CCA ordering quality. We demonstrated that for ultra highly charged CCA adding salt to screen the electrostatic repulsions between colloidal spheres slows the CCA growth kinetics and improves the resolution of the Bragg diffraction interference fringes. For low CCA salt concentrations electrostatic repulsive forces between colloidal particles are large, CCA growth is initially fast and is then readily aborted forming a thin CCA. For increasingly higher CCA salt

concentrations formation of a thicker crystal is achieved. This novel result allows tunability of the CCA thickness. These new understandings of CCA ordering are now being utilized in the development of a highly ordered CCA composed of 50 nm colloidal particles which will be utilized as a UV Raleigh rejection filter for raman scattered light.

In Chapter 3 we solved one of the most vexing problems associated with photon propagation in photonic crystal materials; the physical mechanism for reflection peaks obtained in angularly resolved reflection measurements from the surface photonic crystals. We showed that for two CCA suspensions containing the same colloidal particles but of different colloidal particle number density, we were able to resolve and label the anomalous reflection peaks obtained in an angular geometry to their specific Miller index planes. We proved that these reflection peaks were a result of a multiple diffraction process which consisted of an initial Bragg diffracted beam which was then consecutively 2D diffracted off the set of (111) planes into the (111) specularly reflected direction. We also showed the ability to identify disorder in the CCA by detecting diffracted light from a twinned CCA. This new understanding photon propagation in photonic crystals will allow for the development of novel devices which rely on moulding the flow of light such as light concentrators for solar cell materials.

Chapter 4 details the fabrication and development of a novel non-close-packed inverted photonic crystal material. Non-close-packed inverted structures have the potential to function as 3-dimensional photonic band gap devices. These devices can control, in all three spatial dimensions, the propagation of a defined spectral bandwidth of light. The methods we have developed to fabricate these materials enables the control of the filling fraction of dielectric materials as well as the nearest neighbor particle spacing. This control enables extremely precise tuning of the diffracted spectral bandwidth and Bragg wavelength respectively.

The periodicity in the non-close-packed inverted photonic crystal is templated utilizing a CCA locked inside a hydrogel matrix called a PCCA. The hydrogel backbone of the PCCA expands in the presence of a sol-gel precursor enabling the inorganic material to fill the interstitial space between colloidal particles. Once the sol-gel is condensed we remove the polymeric PCCA through heat treatments which results in an inverted photonic crystal material. We show through pair correlation functions of exposed (111) lattice planes that the non-close-packed inverted photonic crystal is highly ordered. We also show that the CCA template is able to digest colloidal particle polydispersity to maintain long range crystal ordering.